ENGINEERING JOURNAL

Article

Scaled Boundary Finite Element Method for Two-Dimensional Linear Multi-Field Media

Chung Nguyen Van[1,a], Jaroon Rungamornrat[1,b,*], and Phoonsak Pheinsusom[2,c]

1 Applied Mechanics and Structures Research Unit, Department of Civil Engineering, Faculty of Engineering, Chulalongkorn University, Thailand
2 Department of Civil Engineering, Faculty of Engineering, Chulalongkorn University, Thailand
E-mail: [a]nguyenvchung1979@gmail.com, [b]jaroon.r@chula.ac.th (Corresponding author), [c]dr.phoonsak@gmail.com

Abstract. This paper presents an efficient and accurate numerical technique, based on a scaled boundary finite element method (SBFEM) that is capable of solving two-dimensional, second-order, linear, multi-field boundary value problems. Basic governing equations are established in a general, unified context allowing the treatment of various classes of linear problems such as steady-state heat conduction problems, steady-state flow in porous media, linear elasticity, linear piezoelectricity, and linear piezomagnetic and piezoelectromagnetic problems. A scaled boundary finite element approximation is also formulated within a general framework integrating the influence of the distributed body source, general boundary conditions, contributions of the general side-face data, and the flexibility of scaled boundary approximations. Standard procedures for numerical integration, search of eigenvalues and eigenvectors, determination of particular solutions, and solving a system of linear algebraic equations are adopted. After fully tested with available benchmark solutions, the proposed SBFEM is applied to solve various classes of linear problems under different scenarios to demonstrate its vast capability, computational efficiency and robustness.

Keywords: Multi-field problems, SBFEM, surface flux, state variables, scaled boundary coordinates.

ENGINEERING JOURNAL Volume 21 Issue 7
Received 23 June 2017
Accepted 27 August 2017
Published 29 December 2017
Online at http://www.engj.org/
DOI:10.4186/ej.2017.21.7.333

DOI:10.4186/ej.2017.21.7.333

1. Introduction

A scaled boundary finite element method (SBFEM) has been found an attractive alternative analysis tool in the modelling of various problems in applied mechanics for the past two decades [1-12]. The method is recognized as a semi-analytical technique combining features of both analytical schemes and the finite element approximation and, due to the reduction of a spatial dimension in the discretization, it can be also categorized as a particular type of boundary element methods (BEMs). However, the key difference between the SBFEM and conventional BEMs is that the former is generally free of fundamental solutions; as a direct consequence, the non-trivial numerical treatment of singular integrals is not required. The concept of the SBFEM was originally introduced by Wolf and Song [13-15] using the mechanical-based approach to properly and efficiently model linear elastic unbounded media in the dynamic analysis of soil-structure interactions. To further reduce the complexity of the formulation presented in the original work, other techniques such as the standard weighted residual procedure and the principle of virtual work were also utilized to obtain the scaled boundary finite element equations [16-18]. As a result of the computational efficiency of the SBFEM in modelling unbounded media and the reduction of the discretization cost, various researches have been continuously and increasingly conducted, since its first emergence, to introduce other novel aspects and further enhance its capability.

In recent years, the SBFEM has been also applied to solve various boundary value problems. One salient feature of the SBFEM is that the whole domain can be generated by scaling its boundary with respect to a single point termed the scaling center. The SBFEM only requires meshing on a representative boundary of the domain and does not involve fundamental solutions. For a domain with the complex geometries, its interior can be discretized into sub-domains to satisfy the scaling requirement. For fracture problems, the scaling center is commonly located at the crack tip and, as a result, the stress field can be expressed analytically along the direction radiating from the crack tip. As a result, the strength of singularity and associated information can be directly and accurately calculated from the obtained solution [19, 20]. Based on this positive feature, the method has been extensively utilized in the investigation and simulations of fracture problems under various scenarios such as crack formation, static and dynamic crack propagation, and transient responses of bodies containing interfacial cracks, stress singularities and bi-material interfaces [21, 22]. In the modelling of wave propagations, the SBFEM has been also widely employed to study elastic guided waves in an unbounded domain and the radiation and diffraction of linear water waves in shallow water with sidewalls [23-25]. Results from those investigations demonstrated that the SBFEM generally yields more accurate numerical solutions and is more computationally efficient, in terms of the number of degrees of freedom involved, than other existing approaches. Li et al. [26] applied the SBFEM to investigate the structural behavior of offshore monopoles with the influence of the ocean wave loads. The basic concept of the SBFEM was adopted to formulate the governing monopole's equation and the analytical wave equation. Later, Li et al. [6, 7] extended the SBFEM to study three-dimensional wave-pile problems with the emphasis on the wave behavior and pile-group responses. In their formulation, the scaled boundary finite element approximation is applied to Helmholtz equation by separating the vertical component from the velocity potential. The two-dimensional SBFEM was adopted to examine the wave field near the free surface level. Results from these studies indicated that the SBFEM is an accurate and efficient computational tool for the analysis of wave problems and wave-structure interactions. However, their formulation and implementations were still limited to particular settings.

To further enhance the capability of the technique, Deeks and Wolf [27] also integrated an *h*-hierarchical adaptive procedure to the standard SBFEM. This technique exploited the ability of the SBFEM to model the stress singularities at the scaling center and to avoid the discretization of certain adjacent segments of the boundary. Later, Vu and Deeks [28] investigated the performance of high-order elements in the SBFEM. In their study, both the spectral element and hierarchical approaches were employed and they found that the spectral element approach was better than the hierarchical approach in terms of the computational efficiency. Deeks and Augarde [29] also incorporated the meshless scheme into the standard SBFEM to model the far-field problems. Although, the SBFEM has been successfully implemented in various applications, it also possesses certain drawbacks when the number of degrees of freedom resulting from the discretization becomes large, rendering the computational expenses substantial. To overcome such disadvantage, Vu and Deeks [30] integrated a *p*-adaptive scheme in the SBFEM for solving two dimensional boundary value problems. In this study, an alternative set of refinement criteria was considered to maximize the solution accuracy while minimizing the computational cost. Furthermore, He et al. [31] presented a new element-free Galerkin scaled boundary finite element method for the approximation in the

circumferential direction. This particular technique was then applied to solve a number of standard linear elasticity problems and the technique was found to offer higher and better rate of convergence than the original SBFEM. Additionally, He et al. [32] investigated the possibility of using the Fourier shape functions in the SBFEM. The developed technique was then used to solve elastostatics and steady-state heat transfer problems. It was found that the accuracy and convergence of numerical solutions were better than those of results obtained from using the polynomial shape functions and an element-free Galerkin scheme.

Applications of the SBFEM to the analysis of linear problems involving piezoelectric materials have also been recognized in the literature. Liu and Lin [4] used the SBFEM to investigate two-dimensional electrostatic problems. Li et al. [5] developed the SBFEM to solve two-dimensional, linear piezoelectric fracture problems. The stress and electric displacement intensity factors for both static and dynamic cases were calculated directly from results of the SBFEM. It was indicated that the technique requires no asymptotic solution, no local mesh refinement, and no special treatment around the crack tip. Recently, Dieringer and Becker [33] employed the SBFEM to investigate linear problems within the framework of a classical laminated plate theory. In their study, the scaled boundary finite element equations for composites were formulated in terms of the displacement, and the stress singularity at a notch was fully examined. They also demonstrated that the enhanced SBFEM can evaluate the singular stress field as an explicit function of the notch opening displacement. Li et al. [34] and Li et al. [11] also employed the SBFEM to perform two-dimensional simulations of dynamic cracks and interfacial cracks in piezoelectric composites and also study the influence of thermal loads on the fracture response. While the SBFEM has been applied successfully to solve linear piezoelectric problems, the underlying formulation and existing implemented procedures are still limited to certain scenarios and, in particular, the extension of the technique to treat other general coupled-field media has not been found in the literature.

Other recent applications of the SBFEM have been also recognized. For instance, Ooi et al. [9,10] developed an efficient procedure based on the SBFEM together with polygon elements for simulating dynamic crack propagation in elastic media; He et al. [35] presented the SBFEM for the numerical analysis of two-dimensional elastic bodies with the rotationally periodic symmetry and subjected to arbitrary loading conditions; and, most recently, Vu and Deeks [8] integrated the information of the fundamental solutions into the scaled boundary finite element method and then used the technique to investigate problems in linear elasticity with concentrated loads. As become evident from the vast amount of related publications, researches on both the novel development and the enhancement of existing SBFEM have continuously and increasingly grown. However, most of existing SBFEMs were developed specifically for problems considered and this, as a consequence, limits its generality and flexibility to treat general field problems under various scenarios when compared with standard finite element methods. A systematic generalization of the SBFEMs to treat a broader class of boundary value problems obviously requires further rigorous investigations.

The present study aims to offer the SBFEM capable of solving two-dimensional, linear, second-order, multi-field boundary value problems. The key and novel feature is that all basic field equations governing responses of interest are formulated in a general framework allowing various types of linear problems such as steady-state heat conduction and flow in porous media, Laplace's equation, linear elasticity, linear piezoelectricity and other coupled-field problems to be treated in a unified manner. In addition, the treatment of distributed body source, general boundary conditions, prescribed conditions on the side faces, and the scaled boundary approximations are integrated in the implementation.

2. Problem Formulation

Consider a two-dimensional body occupying a region Ω in $\mathbb{R}^2$ as shown schematically in Fig. 1. The region is assumed *smooth* in the sense that all involved mathematical operators (e.g., integrations and differentiations) can be performed on this region. In addition, the boundary of the body Ω, denoted by $\partial\Omega$, is assumed piecewise smooth and an outward unit normal vector at any smooth point on $\partial\Omega$ is denoted by $\boldsymbol{n}=\{n_1 \;\; n_2\}^T$. More restrictions about the geometry of the body Ω pertained in the present study will be posed later as is appropriate. A two-dimensional Cartesian coordinate system $\{\boldsymbol{0};x_1,x_2\}$ with the origin located at point $\boldsymbol{0}$ is introduced and a symbol $f_{,\alpha}$ is used throughout to denote a partial derivative of a function f with respect to the coordinate x_α, $\alpha\in\{1,2\}$ (i.e., $f_{,\alpha}=\partial f/\partial x_\alpha$). Here and in what follows, standard indicial notations apply for subscripts with lower-case Greek and upper-case indices.

DOI:10.4186/ej.2017.21.7.333

In particular, lower-case Greek subscripts range from 1 to 2 whereas upper-case subscripts range from 1 to $\Lambda \in \{1,2,3,...\}$ and repeated subscripts imply the summation over their range unless stated otherwise.

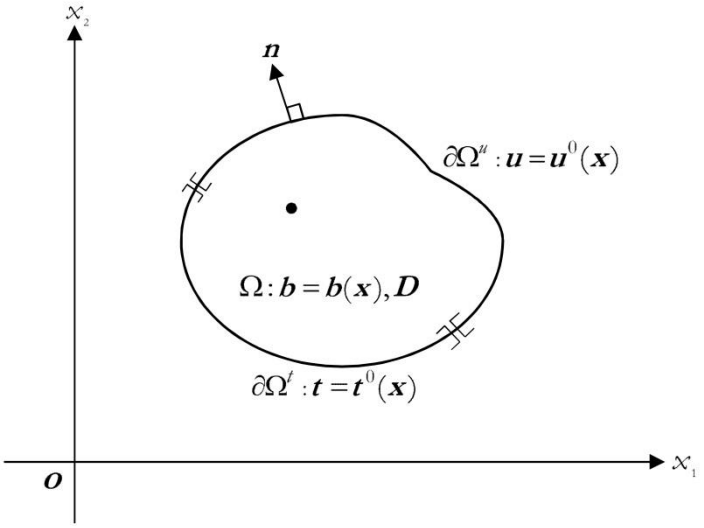

Fig. 1. Schematic of two-dimensional, multi-field body subjected to external excitations.

The body is made of a homogeneous material with its behavior completely characterized by $4\Lambda^2$ constants denoted by a set $\{E_{\alpha I J \beta}\}$ and subjected to a prescribed distributed body-source field, denoted by a Λ-component vector field $\boldsymbol{b}(\boldsymbol{x}) = \{b_1(\boldsymbol{x}) \;\; b_2(\boldsymbol{x}) \; ... \; b_\Lambda(\boldsymbol{x})\}^T$. In the present study, the constants $E_{\alpha I J \beta}$ are assumed to satisfy the symmetry $E_{\alpha I J \beta} = E_{\beta J I \alpha}$. Responses of the body due to the distributed body-source $\boldsymbol{b}(\boldsymbol{x})$ are assumed to be completely described by following three fields: the state variable $\boldsymbol{u}(\boldsymbol{x})$, the state-variable gradient $\bar{\boldsymbol{\varepsilon}}(\boldsymbol{x})$, and the body flux $\boldsymbol{\sigma}(\boldsymbol{x})$. The state variable $\boldsymbol{u}(\boldsymbol{x})$ contains Λ components denoted by $u_J(\boldsymbol{x})$ and is represented, in a vector form, by

$$\boldsymbol{u}(\boldsymbol{x}) = \{u_1(\boldsymbol{x}) \;\; u_2(\boldsymbol{x}) \; ... \; u_\Lambda(\boldsymbol{x})\}^T \tag{1}$$

The state-variable gradient $\bar{\boldsymbol{\varepsilon}}(\boldsymbol{x})$ and the body flux $\boldsymbol{\sigma}(\boldsymbol{x})$ contain 2Λ components denoted by $\bar{\varepsilon}_{\alpha J}$ and $\sigma_{\alpha J}$, respectively, and they can be also represented in a vector form by

$$\bar{\boldsymbol{\varepsilon}}(\boldsymbol{x}) = \{\bar{\varepsilon}_{11}(\boldsymbol{x}) \;\; \bar{\varepsilon}_{12}(\boldsymbol{x}) \; ... \; \bar{\varepsilon}_{1\Lambda}(\boldsymbol{x}) \;\; \bar{\varepsilon}_{21}(\boldsymbol{x}) \;\; \bar{\varepsilon}_{22}(\boldsymbol{x}) \; ... \; \bar{\varepsilon}_{2\Lambda}(\boldsymbol{x})\}^T \tag{2}$$

$$\boldsymbol{\sigma}(\boldsymbol{x}) = \{\sigma_{11}(\boldsymbol{x}) \;\; \sigma_{12}(\boldsymbol{x}) \; ... \; \sigma_{1\Lambda}(\boldsymbol{x}) \;\; \sigma_{21}(\boldsymbol{x}) \;\; \sigma_{22}(\boldsymbol{x}) \; ... \; \sigma_{2\Lambda}(\boldsymbol{x})\}^T \tag{3}$$

In addition, the surface flux at any smooth point $\boldsymbol{x}$ on the boundary is denoted by a Λ-component vector $\boldsymbol{t}(\boldsymbol{x}) = \{t_1(\boldsymbol{x}) \;\; t_2(\boldsymbol{x}) \; ... \; t_\Lambda(\boldsymbol{x})\}^T$. The boundary of the given body $\partial\Omega$ can be decomposed into two disjoint portions; one is denoted by $\partial\Omega^u$ where the state variable $\boldsymbol{u}$ is fully prescribed ($\boldsymbol{u} = \boldsymbol{u}^0(\boldsymbol{x})$ $\forall \boldsymbol{x} \in \partial\Omega^u$ where $\boldsymbol{u}^0(\boldsymbol{x})$ is a prescribed vector) and the other is denoted by $\partial\Omega^t$ where the surface flux $\boldsymbol{t}$ is fully prescribed (i.e., $\boldsymbol{t} = \boldsymbol{t}^0(\boldsymbol{x})$ $\forall \boldsymbol{x} \in \partial\Omega^t$ where $\boldsymbol{t}^0(\boldsymbol{x})$ is a prescribed vector). In the present study, the prescribed vector-value functions $\boldsymbol{b}(\boldsymbol{x})$, $\boldsymbol{u}^0(\boldsymbol{x})$ and $\boldsymbol{t}^0(\boldsymbol{x})$ are assumed sufficiently smooth to ensure the existence of the responses $\boldsymbol{u} = \boldsymbol{u}(\boldsymbol{x})$, $\bar{\boldsymbol{\varepsilon}} = \bar{\boldsymbol{\varepsilon}}(\boldsymbol{x})$ and $\boldsymbol{\sigma} = \boldsymbol{\sigma}(\boldsymbol{x})$.

A set of field equations governing all field quantities described above is formulated within a general framework to allow various classes of linear, second-order, boundary value problems encountered in various areas (e.g., steady-state heat condition problems, steady-state flow in porous media, membrane problems, linear elasticity, problems associated with multi-field materials such as piezoelectric,

piezomagnetic and piezoelectromagnetic solids, etc.) to be treated in a unified manner. The integer Λ is used as a key parameter to indicate the type of problems. For instance, $\Lambda = 1$ corresponds to steady-state heat condition problems, problems of Darcy's flow in porous media, and membrane problems, and $\{\boldsymbol{u}(\boldsymbol{x}); \bar{\boldsymbol{\varepsilon}}(\boldsymbol{x}); \boldsymbol{\sigma}(\boldsymbol{x}); \boldsymbol{b}(\boldsymbol{x}); E_{\alpha I J \beta}; \boldsymbol{t}\}$ represents {temperature; temperature gradient; heat flux; heat source; thermal conductivity; surface heat flux}, {fluid pressure; pressure gradient; fluid flux; source and sink; permeability; surface flux}, and {deflection; slopes; resultant shear force; distributed transverse load; membrane stiffness; end shear force}, respectively; $\Lambda = 2$ corresponds to linear elasticity problems and $\{\boldsymbol{u}(\boldsymbol{x}); \bar{\boldsymbol{\varepsilon}}(\boldsymbol{x}); \boldsymbol{\sigma}(\boldsymbol{x}); \boldsymbol{b}(\boldsymbol{x}); E_{\alpha I J \beta}; \boldsymbol{t}\}$ represents {displacement; displacement gradient; stress; body force; elastic constants; traction}; $\Lambda = 3$ corresponds to linear piezoelectric and piezomagnetic problems and $\{\boldsymbol{u}(\boldsymbol{x}); \bar{\boldsymbol{\varepsilon}}(\boldsymbol{x}); \boldsymbol{\sigma}(\boldsymbol{x}); \boldsymbol{b}(\boldsymbol{x}); E_{\alpha I J \beta}; \boldsymbol{t}\}$ represents {displacement and electric potential; gradients of displacement and electric potential; stress and electric induction; body force and body charge; elastic constants, piezoelectric constants, dielectric permittivities; traction and surface charge} and {displacement and magnetic potential; gradients of displacement and magnetic potential; stress and magnetic induction; body force and magnetic body source; elastic constants, piezomagnetic constants, magnetic permeabilities; traction and surface magnetic induction}, respectively; and $\Lambda = 4$ corresponds to linear piezoelectromagnetic problems and $\{\boldsymbol{u}(\boldsymbol{x}); \bar{\boldsymbol{\varepsilon}}(\boldsymbol{x}); \boldsymbol{\sigma}(\boldsymbol{x}); \boldsymbol{b}(\boldsymbol{x}); E_{\alpha I J \beta}; \boldsymbol{t}\}$ represents {displacement, electric and magnetic potentials; gradients of displacement, electric and magnetic potentials; stress, electric and magnetic inductions; body force, body charge, magnetic body source; elastic, piezoelectric, piezomagnetic and electromagnetic constants, dielectric permittivities, magnetic permeabilities; traction, surface charge, surface magnetic induction}.

The fundamental laws of conservation (e.g., conservation of linear and angular momentum, conservation of mass, conservation of heat flow, etc.), the linear constitutive laws (e.g., Darcy's law, Fourier's law, Hookes' law, generalized Hookes' law, etc), and the laws of kinematics (e.g., strain-displacement relations, electric-potential-field relations, etc.) are employed to form the basic governing field equations and they are expressed in a concise and unified form as follows:

$$\boldsymbol{L}^T \boldsymbol{\sigma} + \boldsymbol{b} = \boldsymbol{0} \tag{4}$$

$$\boldsymbol{\sigma} = \boldsymbol{D} \bar{\boldsymbol{\varepsilon}} \tag{5}$$

$$\bar{\boldsymbol{\varepsilon}} = \boldsymbol{L} \boldsymbol{u} \tag{6}$$

where a superscript "*T*" indicates a matrix transpose operator, $\boldsymbol{D}$ is a $2\Lambda \times 2\Lambda$-matrix termed the modulus matrix, and $\boldsymbol{L}$ represents the linear differential operator defined, in terms of a $2\Lambda \times \Lambda$-matrix, by

$$\boldsymbol{L} = \begin{bmatrix} \boldsymbol{I}_{\Lambda\times\Lambda} \\ \boldsymbol{0}_{\Lambda\times\Lambda} \end{bmatrix} \frac{\partial}{\partial x_1} + \begin{bmatrix} \boldsymbol{0}_{\Lambda\times\Lambda} \\ \boldsymbol{I}_{\Lambda\times\Lambda} \end{bmatrix} \frac{\partial}{\partial x_2} = \boldsymbol{L}_1 \frac{\partial}{\partial x_1} + \boldsymbol{L}_2 \frac{\partial}{\partial x_2};\ \boldsymbol{L}_1 = \begin{bmatrix} \boldsymbol{I}_{\Lambda\times\Lambda} \\ \boldsymbol{0}_{\Lambda\times\Lambda} \end{bmatrix}, \boldsymbol{L}_2 = \begin{bmatrix} \boldsymbol{0}_{\Lambda\times\Lambda} \\ \boldsymbol{I}_{\Lambda\times\Lambda} \end{bmatrix} \tag{7}$$

with $\boldsymbol{I}_{\Lambda\times\Lambda}$ and $\boldsymbol{0}_{\Lambda\times\Lambda}$ denoting a $\Lambda \times \Lambda$-identity matrix and a $\Lambda \times \Lambda$-zero matrix, respectively. It should be remarked that entries of the modulus matrix $\boldsymbol{D}$ can be simply obtained from the set $\{E_{\alpha I J \beta}\}$ by properly considering the definition of the vectors $\boldsymbol{\sigma}$ and $\bar{\boldsymbol{\varepsilon}}$ (i.e., $E_{1JK1} = D_{JK}$, $E_{1JK2} = D_{J,K+\Lambda}$, $E_{2JK1} = D_{J+\Lambda,K}$ and $E_{2JK2} = D_{J+\Lambda,K+\Lambda}$) and, due to the symmetry of $E_{\alpha I J \beta}$, the modulus matrix $\boldsymbol{D}$ is obviously symmetric. By applying the law of conservation at any smooth point $\boldsymbol{x}$ on the boundary $\partial\Omega$, the surface flux $\boldsymbol{t}(\boldsymbol{x})$ can be related to the body flux $\boldsymbol{\sigma}(\boldsymbol{x})$ and the outward unit normal vector $\boldsymbol{n}(\boldsymbol{x}) = \{n_1(\boldsymbol{x}) \ \ n_2(\boldsymbol{x})\}^T$ by

$$\boldsymbol{t} = \begin{bmatrix} n_1 \boldsymbol{I}_{\Lambda\times\Lambda} & n_2 \boldsymbol{I}_{\Lambda\times\Lambda} \end{bmatrix} \boldsymbol{\sigma} \tag{8}$$

Other useful relations such as that directly relating the body flux and the state variable and one connecting the surface flux and the state variable on the boundary can be readily obtained as

$$\boldsymbol{\sigma} = \boldsymbol{D}(\boldsymbol{L}\boldsymbol{u}) \tag{9}$$

DOI:10.4186/ej.2017.21.7.333

$$\boldsymbol{t} = \begin{bmatrix} n_1 \boldsymbol{I}_{\Lambda\times\Lambda} & n_2 \boldsymbol{I}_{\Lambda\times\Lambda} \end{bmatrix} \boldsymbol{D}(\boldsymbol{L}\boldsymbol{u}) \tag{10}$$

2.1. Weak Formulation

A standard weighted residual technique is adopted along with the integration by parts via divergence theorem to obtain a weak-form statement of the above problem. By first taking the inner product of (4) and any sufficiently smooth weight function $\boldsymbol{w}(\boldsymbol{x}) = \{w_1(\boldsymbol{x}) \;\; w_2(\boldsymbol{x}) \; ... \; w_\Lambda(\boldsymbol{x})\}^T$, integrating the result over the body Ω, and then applying an identity $(w_J \sigma_{\alpha J})_{,\alpha} = \boldsymbol{w}^T \boldsymbol{L}^T \boldsymbol{\sigma} + (\boldsymbol{L}\boldsymbol{w})^T \boldsymbol{\sigma}$, it leads to

$$\int_\Omega (\boldsymbol{L}\boldsymbol{w})^T \boldsymbol{\sigma} d\mathcal{A} = \int_\Omega (w_J \sigma_{\alpha J})_{,\alpha} d\mathcal{A} + \int_\Omega \boldsymbol{w}^T \boldsymbol{b} d\mathcal{A} \tag{11}$$

By applying divergence theorem to the first integral on the right hand side (11) and then enforcing the boundary term (8), it gives rise to

$$\int_\Omega (\boldsymbol{L}\boldsymbol{w})^T \boldsymbol{\sigma} d\mathcal{A} = \int_{\partial\Omega} \boldsymbol{w}^T \boldsymbol{t} dl + \int_\Omega \boldsymbol{w}^T \boldsymbol{b} d\mathcal{A} \tag{12}$$

By further replacing the body flux $\boldsymbol{\sigma}$ appearing in (12) by that associated with the state variable via the relation (9), it finally yields

$$\int_\Omega (\boldsymbol{L}\boldsymbol{w})^T \boldsymbol{D}(\boldsymbol{L}\boldsymbol{u}) d\mathcal{A} = \int_{\partial\Omega} \boldsymbol{w}^T \boldsymbol{t} dl + \int_\Omega \boldsymbol{w}^T \boldsymbol{b} d\mathcal{A} \tag{13}$$

It should be apparent from the above formulation that the weak-form Eq. (13) is valid for an arbitrary choice of the weight function $\boldsymbol{w}$. Only restriction placed on the weight function is the smoothness requirement to ensure the integrability of all integrals appearing in (13). This can be achieved by requiring the weight function and their first partial derivatives square integrable, i.e.,

$$\int_\Omega \left[(\boldsymbol{L}\boldsymbol{w})^T (\boldsymbol{L}\boldsymbol{w}) + \boldsymbol{w}^T \boldsymbol{w} \right] d\mathcal{A} < \infty \tag{14}$$

2.2. Scaled Boundary Coordinate Transformation

Let $\boldsymbol{x}_0 = (x_{10}, x_{20})$ be a point in $\mathbb{R}^2$ and C be a simple, piecewise smooth curve in $\mathbb{R}^2$ parameterized by a function $\boldsymbol{r} : s \in [a,b] \rightarrow (x_{10} + \hat{x}_1(s), x_{20} + \hat{x}_2(s)) \in \mathbb{R}^2$ as shown in Fig. 2. Let $\theta(s)$ be the circumferential angle of a point $\boldsymbol{r}(s)$ on the curve C measured from a straight line connecting $\boldsymbol{x}_0$ and $\boldsymbol{r}(a)$ to a straight line connecting $\boldsymbol{x}_0$ and $\boldsymbol{r}(s)$ (see Figure 2). The simple curve C considered here can be either closed (i.e., $\boldsymbol{r}(a) = \boldsymbol{r}(b)$) or opened (i.e., $\boldsymbol{r}(a) \neq \boldsymbol{r}(b)$) and, in addition, it must not contain the point $\boldsymbol{x}_0$ and satisfies the conditions $\theta \in [0, 2\pi]$ and $d\theta/ds > 0 \;\; \forall s \in (a,b)$. Now, let us introduce the following coordinate transformation

$$\boldsymbol{x} = \boldsymbol{x}_0 + \xi \hat{\boldsymbol{x}}(s) \tag{15}$$

where $\xi \geq 0$. It is evident from the coordinate transformation (15) that (i) any straight line $\xi = \xi_0, a \leq s \leq b$ in the $\xi - s$ plane is mapped to a curve S in the $x_1 - x_2$ plane which is simply a scaled version of the curve C about $\boldsymbol{x}_0$ and (ii) any straight line $\xi \geq 0, s = s_0 \in [a,b]$ in the $\xi - s$ plane is mapped to a semi-infinite straight line L in the $x_1 - x_2$ plane starting from $\boldsymbol{x}_0$ and passing through the point $\boldsymbol{r}(s_0)$ on the curve C (also see Figure 2). In addition, a straight line $\xi = 0, a \leq s \leq b$ in the $\xi - s$ plane is mapped to a single point $\boldsymbol{x}_0$ which is termed the *scaling center* and a straight line $\xi = 1, a \leq s \leq b$ in the $\xi - s$ plane is mapped to the

curve C which is termed the *defining curve*. The coordinates ξ and s are termed the *scale boundary coordinates*. Clearly, the transformation (15) maps the region $\xi \geq 0, a \leq s \leq b$ in the $\xi - s$ plane into a region in the $x_1 - x_2$ plane bounded by the two straight lines L_a and L_b (i.e., a shaded region shown in Figure 2). From the coordinate transformation (15), a differential line $d\boldsymbol{\zeta} = \{d\xi \; ds\}^T$ at any point (ξ, s) in the $\xi - s$ plane is related to a differential line $d\boldsymbol{x} = \{dx_1 \; dx_2\}^T$ at any point (x_1, x_2) in the $x_1 - x_2$ plane by

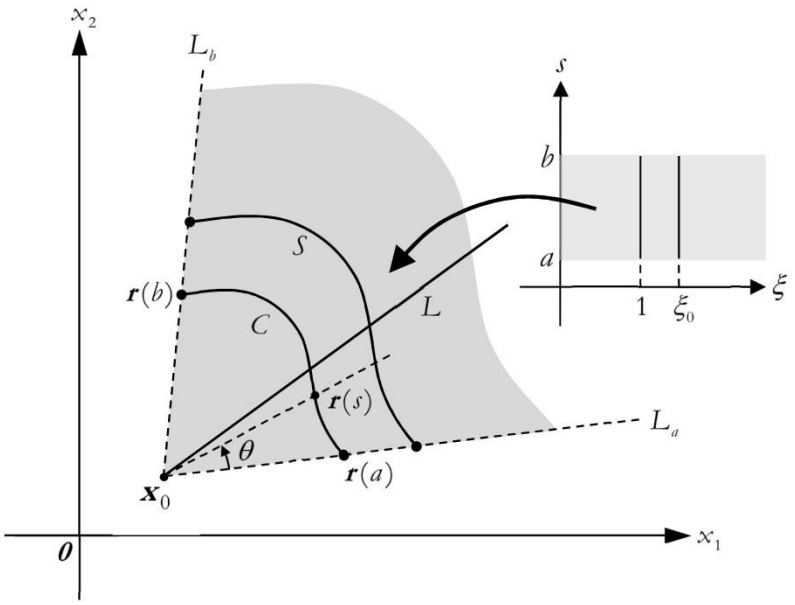

Fig. 2. Schematic of a scaling centre $\boldsymbol{x}_0$ and a defining curve C.

$$d\boldsymbol{x} = \boldsymbol{T} d\boldsymbol{\zeta} = \begin{bmatrix} \hat{x}_1 & \xi d\hat{x}_1/ds \\ \hat{x}_2 & \xi d\hat{x}_2/ds \end{bmatrix} d\xi \; ; \quad d\boldsymbol{\zeta} = \boldsymbol{T}^{-1} d\boldsymbol{x} = \frac{1}{J} \begin{bmatrix} d\hat{x}_2/ds & -d\hat{x}_1/ds \\ -\hat{x}_2/\xi & \hat{x}_1/\xi \end{bmatrix} d\boldsymbol{x} \tag{16}$$

where $J = \hat{x}_1 d\hat{x}_2/ds - \hat{x}_2 d\hat{x}_1/ds$. By setting $d\boldsymbol{\zeta} = (d\lambda)\boldsymbol{m}$ where $\boldsymbol{m}$ is a unit vector and $d\lambda$ is the length of $d\boldsymbol{\zeta}$, it can be readily verified that the length of $d\boldsymbol{x}$, denoted by dl, is given by

$$dl = \sqrt{dx_\alpha dx_\alpha} = \sqrt{T_{\alpha\beta} T_{\alpha\gamma} m_\beta m_\gamma} \, d\lambda \tag{17}$$

For following two special cases: (i) $\boldsymbol{m} = \{1 \; 0\}^T$, $d\lambda = d\xi$ and (ii) $\boldsymbol{m} = \{0 \; 1\}^T$, $d\lambda = ds$, the relation (17) reduces, respectively, to

$$dl = J^\xi(s) d\xi, \;\; J^\xi(s) = \sqrt{\hat{x}_1^2 + \hat{x}_2^2} \tag{18}$$

$$dl = J^s(s) \xi ds, \;\; J^s(s) = \sqrt{\left(d\hat{x}_1/ds\right)^2 + \left(d\hat{x}_2/ds\right)^2} \tag{19}$$

Similarly, the differential area $d\xi ds$ at any point (ξ, s) in the $\xi - s$ plane can be related to the differential area dA at any point (x_1, x_2) in the $x_1 - x_2$ plane by

$$dA = J \xi d\xi ds \tag{20}$$

From the chain rule for differentiations, the partial derivative of any function with respect to the coordinate x_α can be further related to those with respect to the coordinates ξ and s via the following relation

DOI:10.4186/ej.2017.21.7.333

$$\begin{Bmatrix} \dfrac{\partial}{\partial x_1} \\ \dfrac{\partial}{\partial x_2} \end{Bmatrix} = \frac{1}{J}\begin{bmatrix} \dfrac{d\hat{x}_2}{ds} & -\hat{x}_2 \\ -\dfrac{d\hat{x}_1}{ds} & \hat{x}_1 \end{bmatrix}\begin{Bmatrix} \dfrac{\partial}{\partial \xi} \\ \dfrac{1}{\xi}\dfrac{\partial}{\partial s} \end{Bmatrix} \tag{21}$$

The linear differential operator $\boldsymbol{L}$ given by (7) can be now expressed in terms of partial derivatives with respect to the coordinates ξ and s by

$$\boldsymbol{L} = \boldsymbol{b}_1 \frac{\partial}{\partial \xi} + \boldsymbol{b}_2 \frac{1}{\xi}\frac{\partial}{\partial s} \tag{22}$$

where $\boldsymbol{b}_1$ and $\boldsymbol{b}_2$ are $2\Lambda \times \Lambda$-matrices defined by

$$\boldsymbol{b}_1 = \frac{1}{J}\begin{bmatrix} \dfrac{d\hat{x}_2}{ds}\boldsymbol{I}_{\Lambda\times\Lambda} \\ -\dfrac{d\hat{x}_1}{ds}\boldsymbol{I}_{\Lambda\times\Lambda} \end{bmatrix}, \quad \boldsymbol{b}_2 = \frac{1}{J}\begin{bmatrix} -\hat{x}_2\boldsymbol{I}_{\Lambda\times\Lambda} \\ \hat{x}_1\boldsymbol{I}_{\Lambda\times\Lambda} \end{bmatrix} \tag{23}$$

In the present study, we focus only on a body Ω whose geometry can be completely described by a single scaling center. In particular, there must exist the scaling center $\boldsymbol{x}_0$ and defining curve C such that there exists a region $[\xi_1,\xi_2]\times[s_1,s_2]$ in the $\xi - s$ plane that is mapped into the region Ω in the $x_1 - x_2$ plane via the transformation (15). If the defining curve C is opened, the body is said to be *opened* and portions of the boundary $\partial\Omega$ associated with $s = s_1$ and $s = s_2$ are termed the *side faces* (see Figure 3(a), (b), (c) and (d)). If the defining curve is closed, the body is said to be closed and the boundary $\partial\Omega$ contains no side face (see Figure 3(e), (f), (g) and (h)). If ξ_2 is finite, the body Ω is said to be bounded (see Figures 3(a), (c), (e) and (g)); otherwise (i.e., $\xi_2 = \infty$), it is said to be unbounded (see Figures 3(b), (d), (f) and (h)). If $\xi_1 = 0$, the body Ω contains the scaling center $\boldsymbol{x}_0$ (see Figures 3(c), (d), (g) and (h)); otherwise (i.e., $\xi_1 > 0$), the body Ω does not contain the scaling center $\boldsymbol{x}_0$ (see Figures 3(a), (b), (e) and (f)). Portions of the boundary $\partial\Omega$ associated with $\xi = \xi_1 > 0$ and $\xi = \xi_2 < \infty$ are termed the inner and outer boundaries, respectively.

2.3. Scaled Boundary Finite Element Approximation

The defining curve C is discretized into a mesh containing n elements and m nodes. The coordinates of any point on C, denoted by $\boldsymbol{x} = \boldsymbol{x}_0 + \hat{\boldsymbol{x}}(s)$, is then approximated by

$$x_\alpha^h(s) = x_{\alpha 0} + \sum_{i=1}^{m} \phi_{(i)}(s)\hat{x}_{\alpha(i)} = x_{\alpha 0} + \boldsymbol{N}^G\boldsymbol{X}_\alpha \tag{24}$$

where the superscript "h" is used, here and in what follows, to designate approximate quantities, $\boldsymbol{N}^G = \{\phi_{(1)} \quad \phi_{(2)} \quad \cdots \quad \phi_{(m)}\}$ stands for a row-matrix containing all nodal basis functions, and $\boldsymbol{X}_\alpha = \{\hat{x}_{\alpha(1)} \quad \hat{x}_{\alpha(2)} \quad \cdots \quad \hat{x}_{\alpha(m)}\}^T$ denotes a vector containing all nodal relative coordinates in which $\hat{x}_{\alpha(i)} = x_{\alpha(i)} - x_{\alpha 0}$ represents the coordinate of the i^{th} node relative to the scaling center $\boldsymbol{x}_0$. The resulting discretized defining curve is denoted by C^h and the region in the $x_1 - x_2$ plane described by the discretized defining curve C^h is then used as the approximation for the geometry of the body Ω and denoted by Ω^h. With the relation (24), the derivative $d\hat{x}_\alpha / ds$ is then approximated by

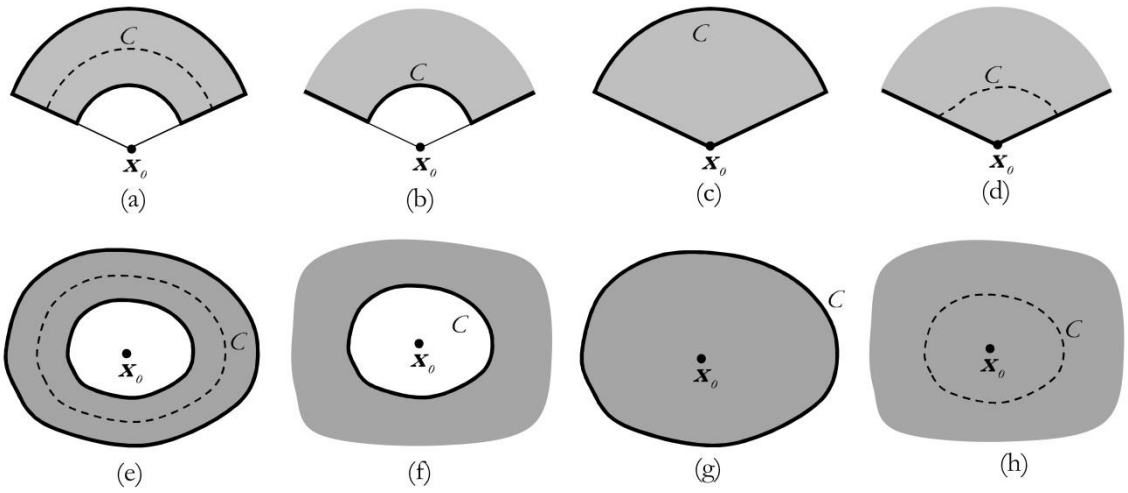

Fig. 3. Schematics of opened bodies: (a) bounded body containing no scaling center, (b) unbounded body containing no scaling center, (c) bounded body containing scaling center, and (d) unbounded body containing scaling center, and schematics of closed bodies: (e) bounded body containing a hole, (f) unbounded body containing a hole, (g) bounded body containing no hole, and (h) unbounded body containing no hole.

$$\frac{d\hat{x}_\alpha^h}{ds} = \boldsymbol{B}^G \boldsymbol{X}_\alpha \tag{25}$$

where $\boldsymbol{B}^G = d\boldsymbol{N}^G/ds$. Approximations of J, J^ξ, J^s, $\boldsymbol{b}_1$, $\boldsymbol{b}_2$ and the linear operator $\boldsymbol{L}$ are given by

$$J^h = \boldsymbol{X}_1^T(\boldsymbol{N}^G)^T\boldsymbol{B}^G\boldsymbol{X}_2 - \boldsymbol{X}_2^T(\boldsymbol{N}^G)^T\boldsymbol{B}^G\boldsymbol{X}_1 \tag{26}$$

$$J^{\xi h} = \sqrt{\boldsymbol{X}_1^T(\boldsymbol{N}^G)^T\boldsymbol{N}^G\boldsymbol{X}_1 + \boldsymbol{X}_2^T(\boldsymbol{N}^G)^T\boldsymbol{N}^G\boldsymbol{X}_2}\,,\ J^{sh} = \sqrt{\boldsymbol{X}_1^T(\boldsymbol{B}^G)^T\boldsymbol{B}^G\boldsymbol{X}_1 + \boldsymbol{X}_2^T(\boldsymbol{B}^G)^T\boldsymbol{B}^G\boldsymbol{X}_2} \tag{27}$$

$$\boldsymbol{b}_1^h = \frac{1}{J^h}\begin{bmatrix}\boldsymbol{B}^G\boldsymbol{X}_2\boldsymbol{I}_{\Lambda\times\Lambda}\\ -\boldsymbol{B}^G\boldsymbol{X}_1\boldsymbol{I}_{\Lambda\times\Lambda}\end{bmatrix},\quad \boldsymbol{b}_2^h = \frac{1}{J^h}\begin{bmatrix}-\boldsymbol{N}^G\boldsymbol{X}_2\boldsymbol{I}_{\Lambda\times\Lambda}\\ \boldsymbol{N}^G\boldsymbol{X}_1\boldsymbol{I}_{\Lambda\times\Lambda}\end{bmatrix} \tag{28}$$

$$\boldsymbol{L}^h = \boldsymbol{b}_1^h\frac{\partial}{\partial\xi} + \boldsymbol{b}_2^h\frac{1}{\xi}\frac{\partial}{\partial s} \tag{29}$$

From the coordinate transformation (15) along with the approximation (24), the state variable $\boldsymbol{u}$ and the weight function $\boldsymbol{w}$ are now approximated, respectively, by $\boldsymbol{u}^h$ and $\boldsymbol{w}^h$ in a form

$$\boldsymbol{u}^h = \boldsymbol{u}^h(\xi,s) = \sum_{i=1}^{m}\varphi_{(i)}(s)\boldsymbol{u}_{(i)}^h(\xi) = \boldsymbol{N}^S\boldsymbol{U}^h \tag{30}$$

$$\boldsymbol{w}^h = \boldsymbol{w}^h(\xi,s) = \sum_{i=1}^{m}\varphi_{(i)}(s)\boldsymbol{w}_{(i)}^h(\xi) = \boldsymbol{N}^S\boldsymbol{W}^h \tag{31}$$

where $\boldsymbol{u}_{(i)}^h(\xi)$ and $\boldsymbol{w}_{(i)}^h(\xi)$ denote values of the state variable and arbitrary function along the line $s = s_{(i)}$, respectively; $\boldsymbol{N}^S = \{\varphi_{(1)}\boldsymbol{I}_{\Lambda\times\Lambda}\quad \varphi_{(2)}\boldsymbol{I}_{\Lambda\times\Lambda}\quad\cdots\quad \varphi_{(m)}\boldsymbol{I}_{\Lambda\times\Lambda}\}$ is a $\Lambda\times m\Lambda$ -matrix containing all nodal basis functions; and $\boldsymbol{U}^h = \{\boldsymbol{u}_{(1)}^h(\xi)\quad \boldsymbol{u}_{(2)}^h(\xi)\quad\cdots\quad \boldsymbol{u}_{(m)}^h(\xi)\}^T$ and $\boldsymbol{W}^h = \{\boldsymbol{w}_{(1)}^h(\xi)\quad \boldsymbol{w}_{(2)}^h(\xi)\quad\cdots\quad \boldsymbol{w}_{(m)}^h(\xi)\}^T$ denote vectors containing all functions $\boldsymbol{u}_{(i)}^h(\xi)$ and $\boldsymbol{w}_{(i)}^h(\xi)$, respectively. It should be remarked that the nodal basis functions $\phi_{(i)}(s)$ and $\varphi_{(i)}(s)$ are constructed using a finite element technique by simply

DOI:10.4186/ej.2017.21.7.333

patching the local element shape functions associated with the i^{th} node and, as a result, it satisfies the Kronecker-delta property, i.e., $\phi_{(i)}(s_{(j)}) = \varphi_{(i)}(s_{(j)}) = \delta_{ij}$ where $s_{(j)}$ is the value of the boundary coordinate s of the j^{th} node and δ_{ij} denotes the Kronecker-delta symbol. The approximation of the body flux $\boldsymbol{\sigma}$ and $\boldsymbol{Lw}$ at any point $\boldsymbol{x} \in \Omega^h$ in the $x_1 - x_2$ plane can also be obtained by

$$\boldsymbol{\sigma}^h = \boldsymbol{\sigma}^h(\xi, s) = \boldsymbol{D}(\boldsymbol{L}^h \boldsymbol{u}^h) = \boldsymbol{D}\left[\boldsymbol{b}_1^h \frac{\partial}{\partial \xi} + \boldsymbol{b}_2^h \frac{1}{\xi}\frac{\partial}{\partial s}\right](\boldsymbol{N}^S \boldsymbol{U}^h) = \boldsymbol{D}\left[\boldsymbol{B}_1 \boldsymbol{U}_{,\xi}^h + \frac{1}{\xi}\boldsymbol{B}_2 \boldsymbol{U}^h\right] \tag{32}$$

$$\boldsymbol{L}^h \boldsymbol{w}^h = \boldsymbol{L}^h \boldsymbol{w}^h(\xi, s) = \left[\boldsymbol{b}_1^h \frac{\partial}{\partial \xi} + \boldsymbol{b}_2^h \frac{1}{\xi}\frac{\partial}{\partial s}\right](\boldsymbol{N}^S \boldsymbol{W}^h) = \left[\boldsymbol{B}_1 \boldsymbol{W}_{,\xi}^h + \frac{1}{\xi}\boldsymbol{B}_2 \boldsymbol{W}^h\right] \tag{33}$$

where $\boldsymbol{B}_1$ and $\boldsymbol{B}_2$ are defined by

$$\boldsymbol{B}_1 = \boldsymbol{b}_1^h \boldsymbol{N}^S, \quad \boldsymbol{B}_2 = \boldsymbol{b}_2^h \boldsymbol{B}^S = \boldsymbol{b}_2^h d\boldsymbol{N}^S / ds \tag{34}$$

It is worth noting that both the matrices $\boldsymbol{B}_1$ and $\boldsymbol{B}_2$ are independent of the scaling coordinate ξ.

2.4. Scaled Boundary Finite Element Equations

A set of scaled boundary finite element equations is established, here, for a generic, two-dimensional body Ω as shown in Figure 4 to ensure that the resulting formulation is applicable to various cases. The boundary of the domain $\partial\Omega$ is assumed consisting of four parts resulting from the scale boundary coordinate transformation with the scaling center $\boldsymbol{x}_0$ and defining curve C : the inner boundary $\partial\Omega_1$, the outer boundary $\partial\Omega_2$, the side-face-1 $\partial\Omega_1^s$, and the side-face-2 $\partial\Omega_2^s$. For certain special cases such as closed bodies without the side face, bodies containing the scaling center, and unbounded bodies, it simply takes $\partial\Omega_1^s = \partial\Omega_2^s = \varnothing$, $\partial\Omega_1 = \varnothing$, and $\partial\Omega_2 = \varnothing$ in the following formulation, respectively. The approximation of the given body Ω is achieved via the discretization of the defining curve C^h along with the mapping region $[\xi_1, \xi_2] \times [s_1, s_2]$ in the $\xi - s$ plane, and the approximate body is denoted by Ω^h. In particular, the approximate inner and outer boundaries $\partial\Omega_1^h$ and $\partial\Omega_2^h$, the side-face-1 $\partial\Omega_1^s$, and the side-face-2 $\partial\Omega_2^s$ are fully described by a curve $\xi = \xi_1, s_1 \le s \le s_2$, a curve $\xi = \xi_2, s_1 \le s \le s_2$, a straight line $s = s_1, \xi_1 \le \xi \le \xi_2$, and a straight line $s = s_2, \xi_1 \le \xi \le \xi_2$, respectively.

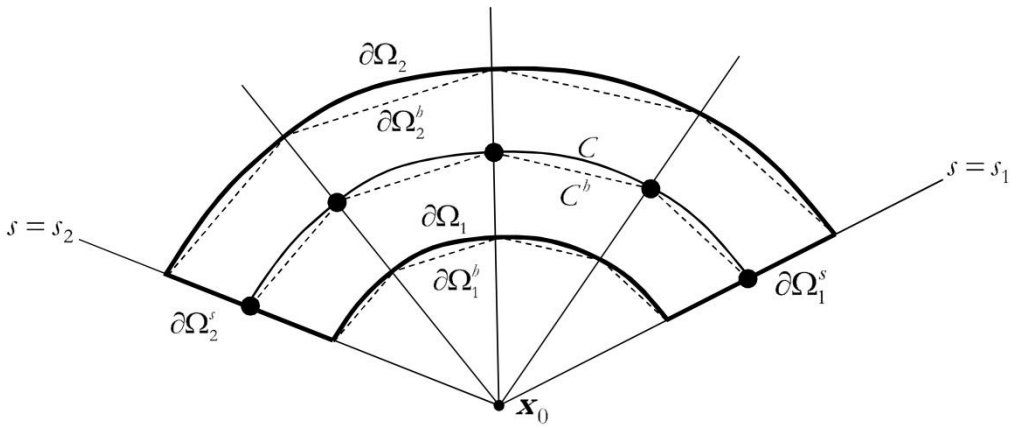

Fig. 4. Schematic of a generic body Ω and its approximation Ω^h. The dashed lines are used to represent the approximation of the defining curve, the inner boundary and the outer boundary.

From the boundary partition $\partial\Omega = \partial\Omega_1 \cup \partial\Omega_2 \cup \partial\Omega_1^s \cup \partial\Omega_1^s$ and the coordinate transformation (15), the weak-form equation (13) can be rewritten for this generic body Ω as

$$\begin{aligned}\int_{s_1}^{s_2}\int_{\xi_1}^{\xi_2} (\boldsymbol{L}\boldsymbol{w})^T \boldsymbol{D}(\boldsymbol{L}\boldsymbol{u}) J \xi d\xi ds = \int_{s_1}^{s_2}\int_{\xi_1}^{\xi_2} \boldsymbol{w}^T \boldsymbol{b} J \xi d\xi ds + \int_{s_1}^{s_2} \boldsymbol{w}_1^T \boldsymbol{t}_1(s) J^s(s) \xi_1 ds + \int_{s_1}^{s_2} \boldsymbol{w}_2^T \boldsymbol{t}_2(s) J^s(s) \xi_2 ds \\ + \int_{\xi_1}^{\xi_2} (\boldsymbol{w}_1^s)^T \boldsymbol{t}_1^s(\xi) J_1^\xi d\xi + \int_{\xi_1}^{\xi_2} (\boldsymbol{w}_2^s)^T \boldsymbol{t}_2^s(\xi) J_2^\xi d\xi\end{aligned} \tag{35}$$

where $\boldsymbol{w}_1$, $\boldsymbol{w}_2$, $\boldsymbol{w}_1^s$, $\boldsymbol{w}_2^s$ are restrictions of the weight function $\boldsymbol{w}$ on the boundaries $\partial\Omega_1$, $\partial\Omega_2$, $\partial\Omega_1^s$, $\partial\Omega_2^s$, respectively; $\boldsymbol{t}_1$, $\boldsymbol{t}_2$, $\boldsymbol{t}_1^s$, $\boldsymbol{t}_2^s$ are surface flux on the boundaries $\partial\Omega_1$, $\partial\Omega_2$, $\partial\Omega_1^s$, $\partial\Omega_2^s$, respectively; and $J_1^\xi = J^\xi(s_1)$, $J_2^\xi = J^\xi(s_2)$. Next, by introducing the approximations of the body flux (32) and the derivatives of the weight function (33) along with the domain approximation, the integral on the left-hand side of (35), denoted for convenience by $\mathcal{I}_1$, becomes

$$\begin{aligned}\mathcal{I}_1 = \int_{s_1}^{s_2}\int_{\xi_1}^{\xi_2} (\boldsymbol{W}_{,\xi}^h)^T \boldsymbol{B}_1^T \boldsymbol{D} \boldsymbol{B}_1 \boldsymbol{U}_{,\xi}^h J^h \xi d\xi ds + \int_{s_1}^{s_2}\int_{\xi_1}^{\xi_2} (\boldsymbol{W}_{,\xi}^h)^T \boldsymbol{B}_1^T \boldsymbol{D} \boldsymbol{B}_2 \boldsymbol{U}^h J^h d\xi ds \\ + \int_{s_1}^{s_2}\int_{\xi_1}^{\xi_2} (\boldsymbol{W}^h)^T \boldsymbol{B}_2^T \boldsymbol{D} \boldsymbol{B}_1 \boldsymbol{U}_{,\xi}^h J^h d\xi ds + \int_{s_1}^{s_2}\int_{\xi_1}^{\xi_2} (\boldsymbol{W}^h)^T \boldsymbol{B}_2^T \boldsymbol{D} \boldsymbol{B}_2 \boldsymbol{U}^h \frac{J^h}{\xi} d\xi ds\end{aligned} \tag{36}$$

Further integrating the first two integrals by parts with respect to the coordinate ξ and recalling that the matrices $\boldsymbol{B}_1$ and $\boldsymbol{B}_2$ are independent of the coordinate ξ, $\boldsymbol{W}^h$ and $\boldsymbol{U}^h$ are independent of the coordinate s, and the matrix $\boldsymbol{D}$ is independent of both ξ and s, the integral $\mathcal{I}_1$ is simplified to

$$\begin{aligned}\mathcal{I}_1 = \int_{\xi_1}^{\xi_2} (\boldsymbol{W}^h)^T \left[-\xi \boldsymbol{E}_0 \boldsymbol{U}_{,\xi\xi}^h + (\boldsymbol{E}_1 - \boldsymbol{E}_1^T - \boldsymbol{E}_0) \boldsymbol{U}_{,\xi}^h + \frac{1}{\xi} \boldsymbol{E}_2 \boldsymbol{U}^h \right] d\xi \\ + (\boldsymbol{W}_2^h)^T \left\{ \xi \boldsymbol{E}_0 \boldsymbol{U}_{,\xi}^h + \boldsymbol{E}_1^T \boldsymbol{U}^h \right\}_{\xi=\xi_2} - (\boldsymbol{W}_1^h)^T \left\{ \xi \boldsymbol{E}_0 \boldsymbol{U}_{,\xi}^h + \boldsymbol{E}_1^T \boldsymbol{U}^h \right\}_{\xi=\xi_1}\end{aligned} \tag{37}$$

where $\boldsymbol{W}_1^h = \boldsymbol{W}^h(\xi = \xi_1)$, $\boldsymbol{W}_2^h = \boldsymbol{W}^h(\xi = \xi_2)$, and $\boldsymbol{E}_0$, $\boldsymbol{E}_1$, and $\boldsymbol{E}_2$ are defined by

$$\boldsymbol{E}_0 = \int_{s_1}^{s_2} \boldsymbol{B}_1^T \boldsymbol{D} \boldsymbol{B}_1 J^h ds, \quad \boldsymbol{E}_1 = \int_{s_1}^{s_2} \boldsymbol{B}_2^T \boldsymbol{D} \boldsymbol{B}_1 J^h ds, \quad \boldsymbol{E}_2 = \int_{s_1}^{s_2} \boldsymbol{B}_2^T \boldsymbol{D} \boldsymbol{B}_2 J^h ds \tag{38}$$

It is evident that both matrices $\boldsymbol{E}_0$ and $\boldsymbol{E}_2$ are symmetric. By following a similar procedure, the boundary integrals appearing on the right-hand side of (35), denoted by $\mathcal{I}_2$, can be approximated by

$$\mathcal{I}_2 = (\boldsymbol{W}_1^h)^T \boldsymbol{P}_1 + (\boldsymbol{W}_2^h)^T \boldsymbol{P}_2 + \int_{\xi_1}^{\xi_2} (\boldsymbol{W}^h)^T \boldsymbol{F}_1^t d\xi + \int_{\xi_1}^{\xi_2} (\boldsymbol{W}^h)^T \boldsymbol{F}_2^t d\xi \tag{39}$$

where $\boldsymbol{N}_1^S = \boldsymbol{N}^S(s = s_1)$, $\boldsymbol{N}_2^S = \boldsymbol{N}^S(s = s_2)$, and

$$\boldsymbol{P}_1 = \int_{s_1}^{s_2} (\boldsymbol{N}^S)^T \boldsymbol{t}_1(s) \xi_1 J^{sh}(s) ds, \quad \boldsymbol{P}_2 = \int_{s_1}^{s_2} (\boldsymbol{N}^S)^T \boldsymbol{t}_2(s) \xi_2 J^{sh}(s) ds \tag{40}$$

$$\boldsymbol{F}_1^t = (\boldsymbol{N}_1^S)^T \boldsymbol{t}_1^s(\xi) J_1^{\xi h}, \quad \boldsymbol{F}_2^t = (\boldsymbol{N}_2^S)^T \boldsymbol{t}_2^s(\xi) J_2^{\xi h} \tag{41}$$

in which $J_1^{\xi b} = J^{\xi b}(s_1)$ and $J_2^{\xi b} = J^{\xi b}(s_2)$. Without loss of generality, the *first* and *last* nodes resulting from the discretization of opened bodies are taken as a node on the side-face-1 and a node on the side-face-2, respectively, and this applies in what follows. It should be remarked from the Kronecker property of the nodal basis functions that $\varphi_{(1)}(s_1)=1$, $\varphi_{(j)}(s_1)=0\ \forall j\geq 2$ and $\varphi_{(m)}(s_2)=1$, $\varphi_{(j)}(s_2)=0\ \forall j\leq m-1$. Now, both the matrices $\boldsymbol{N}_1^S$ and $\boldsymbol{N}_2^S$ clearly contain many zero entries and simply take the form

$$\boldsymbol{N}_1^S=\{\boldsymbol{I}_{\Lambda\times\Lambda}\quad \boldsymbol{0}_{\Lambda\times\Lambda}\quad \cdots\quad \boldsymbol{0}_{\Lambda\times\Lambda}\},\quad \boldsymbol{N}_2^S=\{\boldsymbol{0}_{\Lambda\times\Lambda}\quad \boldsymbol{0}_{\Lambda\times\Lambda}\quad \cdots\quad \boldsymbol{I}_{\Lambda\times\Lambda}\} \tag{42}$$

Substituting (42) into (41) leads to

$$\boldsymbol{F}_1^t=\{J_1^{\xi b}\boldsymbol{t}_1^s(\xi)\quad \boldsymbol{0}_\Lambda\quad \cdots\quad \boldsymbol{0}_\Lambda\}^T,\quad \boldsymbol{F}_2^t=\{\boldsymbol{0}_\Lambda\quad \boldsymbol{0}_\Lambda\quad \cdots\quad J_2^{\xi b}\boldsymbol{t}_2^s(\xi)\}^T \tag{43}$$

where $\boldsymbol{0}_\Lambda$ is a zero Λ-component vector. Finally, the domain integral associated with the distributed body source on the right-hand side of (35), denoted by $\mathcal{J}_3$, can be approximated by

$$\mathcal{J}_3=\int_{\xi_1}^{\xi_2}(\boldsymbol{W}^b)^T\xi\boldsymbol{F}^b d\xi \tag{44}$$

where the matrix $\boldsymbol{F}^b$ is defined by

$$\boldsymbol{F}^b=\int_{s_1}^{s_2}(\boldsymbol{N}^S)^T\boldsymbol{b}J^b ds=\left\{\int_{s_1}^{s_2}\phi_{(1)}\boldsymbol{b}J^b ds\quad \int_{s_1}^{s_2}\phi_{(2)}\boldsymbol{b}J^b ds\quad \cdots\quad \int_{s_1}^{s_2}\phi_{(m)}\boldsymbol{b}J^b ds\right\}^T \tag{45}$$

By combing the results (37), (39) and (44), the approximation of the weak-form (35) becomes

$$\begin{aligned}&\int_{\xi_1}^{\xi_2}(\boldsymbol{W}^b)^T\left[-\xi\boldsymbol{E}_0\boldsymbol{U}^b_{,\xi\xi}+(\boldsymbol{E}_1-\boldsymbol{E}_1^T-\boldsymbol{E}_0)\boldsymbol{U}^b_{,\xi}+\frac{1}{\xi}\boldsymbol{E}_2\boldsymbol{U}^b-\boldsymbol{F}^t-\xi\boldsymbol{F}^b\right]d\xi\\&+(\boldsymbol{W}_2^b)^T\left[\left\{\xi\boldsymbol{E}_0\boldsymbol{U}^b_{,\xi}+\boldsymbol{E}_1^T\boldsymbol{U}^b\right\}_{\xi=\xi_2}-\boldsymbol{P}_2\right]-(\boldsymbol{W}_1^b)^T\left[\left\{\xi\boldsymbol{E}_0\boldsymbol{U}^b_{,\xi}+\boldsymbol{E}_1^T\boldsymbol{U}^b\right\}_{\xi=\xi_1}+\boldsymbol{P}_1\right]=0\end{aligned} \tag{46}$$

where $\boldsymbol{F}^t=\boldsymbol{F}_1^t+\boldsymbol{F}_2^t$. From the arbitrariness of the weight function $\boldsymbol{W}^b$, it can be deduced that

$$\xi^2\boldsymbol{E}_0\boldsymbol{U}^b_{,\xi\xi\xi}+\xi(\boldsymbol{E}_0+\boldsymbol{E}_1^T-\boldsymbol{E}_1)\boldsymbol{U}^b_{,\xi}-\boldsymbol{E}_2\boldsymbol{U}^b+\xi\boldsymbol{F}^t+\xi^2\boldsymbol{F}^b=\boldsymbol{0}\quad \forall\xi\in(\xi_1,\xi_2) \tag{47}$$

$$\boldsymbol{Q}^b(\xi_1)=-\boldsymbol{P}_1 \tag{48}$$

$$\boldsymbol{Q}^b(\xi_2)=\boldsymbol{P}_2 \tag{49}$$

where the vector $\boldsymbol{Q}^b=\boldsymbol{Q}^b(\xi)$ known as the nodal internal flux is defined by

$$\boldsymbol{Q}^b(\xi)=\xi\boldsymbol{E}_0\boldsymbol{U}^b_{,\xi}+\boldsymbol{E}_1^T\boldsymbol{U}^b \tag{50}$$

A set of Eqs. (47)-(49) is known as the scaled boundary finite element equations governing the unknown function $\boldsymbol{U}^b=\boldsymbol{U}^b(\xi)$. It can be remarked that (47) forms a system of linear, second-order, nonhomogeneous, ordinary differential equations with respect to the coordinate ξ whereas (48) and (49) pose the boundary conditions on both inner and outer boundaries of the body. As previously pointed out, the governing equations and boundary conditions (47)-(49) are formulated in a general context; as a result, for certain special cases, some terms or equations must be eliminated properly. For instances, the boundary

condition (49) is ignored for unbounded bodies; the boundary condition (48) is ignored for bounded bodies containing the scaling center; the term $\boldsymbol{F}^t$ vanishes for closed bodies; and the term $\boldsymbol{F}^b$ vanishes for bodies free of the distributed body source.

2.5. Treatment of Prescribed Conditions on Side Faces

It should be evident from (47)-(49) that the information associated with the prescribed distributed body source and the prescribed boundary conditions on both inner and outer boundaries can be integrated into the formulation via the term $\boldsymbol{F}^b$ and the boundary conditions (48)-(49), respectively. However, the consideration of the prescribed surface flux and state variable on the side face is still not apparent from the above formulation. The system of linear differential equations (47) can be further re-expressed in a form well-suited for the treatment of those prescribed side-face conditions.

First, bodies considered in the present study are divided into five groups, *Group*-1, *Group*-2, *Group*-3, *Group*-4, and *Group*-5, associated with closed bodies without the side-face, opened bodies with prescribed surface flux on both side faces, opened bodies with prescribed surface flux on the side-face-1 and prescribed state variable on the side-face-2, opened bodies with prescribed surface flux on the side-face-2 and prescribed state variable on the side-face-1, and opened bodies with prescribed state variable on both side faces, respectively. For bodies in *Group*-1, $\boldsymbol{U}^b$ contains only unknown functions and $\boldsymbol{t}_1^s$, $\boldsymbol{t}_2^s$ disappear; for bodies in *Group*-2, $\boldsymbol{U}^b$ contains only unknown functions whereas $\boldsymbol{t}_1^s$, $\boldsymbol{t}_2^s$ are fully prescribed; for bodies in *Group*-3, $\boldsymbol{t}_1^s$, and $\boldsymbol{u}_{(m)}^b(\xi)$ are fully prescribed and $\boldsymbol{t}_2^s$ and the remaining functions $\boldsymbol{u}_{(i)}^b(\xi)\ \forall i \le m-1$ in $\boldsymbol{U}^b$ are unknown; for bodies in *Group*-4, $\boldsymbol{t}_2^s$ and $\boldsymbol{u}_{(1)}^b(\xi)$ are fully prescribed and $\boldsymbol{t}_1^s$ and the remaining functions $\boldsymbol{u}_{(i)}^b(\xi)\ \forall i \ge 2$ in $\boldsymbol{U}^b$ are unknown; and for bodies in *Group*-5, both $\boldsymbol{u}_{(1)}^b(\xi)$ and $\boldsymbol{u}_{(m)}^b(\xi)$ are fully prescribed whereas $\boldsymbol{t}_1^s$, $\boldsymbol{t}_2^s$, and the remaining functions $\boldsymbol{u}_{(i)}^b(\xi)\ \forall 2 \le i \le m-1$ in $\boldsymbol{U}^b$ are unknown. To treat the prescribed conditions on the side-face for bodies in all groups, the vector $\boldsymbol{U}^b$ is partitioned and rearranged into known and unknown parts as $\boldsymbol{U}^b = \{\boldsymbol{U}^{bu} \quad \boldsymbol{U}^{bc}\}^T$ where $\boldsymbol{U}^{bu} = \boldsymbol{U}^{bu}(\xi)$ contains only unknown functions from a collection $\boldsymbol{u}_{(i)}^b(\xi), i = 1,2,...,m$ and $\boldsymbol{U}^{bc} = \boldsymbol{U}^{bc}(\xi)$ contains the remaining known functions associated with the prescribed state variable on the side face. By defining p as the number of known functions $\boldsymbol{u}_{(i)}^b(\xi)$ contained in $\boldsymbol{U}^{bc}$, the number of remaining unknown functions $\boldsymbol{u}_{(i)}^b(\xi)$ contained in $\boldsymbol{U}^{bu}$ is therefore equal to $m-p$. Clearly, the value of p associated with bodies in *Group*-1, *Group*-2, *Group*-3, *Group*-4, and *Group*-5 are 0, 0, 1, 1, and 2 respectively. Consistent with the partition of the vector $\boldsymbol{U}^b$, the vector $\boldsymbol{F}^t$ can be also partitioned into $\boldsymbol{F}^t = \{\boldsymbol{F}^{tu} \quad \boldsymbol{F}^{tc}\}^T$ where $\boldsymbol{F}^{tu} = \boldsymbol{F}^{tu}(\xi)$ contains many zero functions and known functions corresponding to the prescribed surface flux on the side face and $\boldsymbol{F}^{tc} = \boldsymbol{F}^{tc}(\xi)$ contains unknown functions associated with the unknown surface flux on the side face. According to this partition, the system of differential equations (47) can be separated into

$$\xi^2 \boldsymbol{E}_0^{uu} \boldsymbol{U}_{,\xi\xi}^{bu} + \xi\left[\boldsymbol{E}_0^{uu} + (\boldsymbol{E}_1^{uu})^T - \boldsymbol{E}_1^{uu}\right]\boldsymbol{U}_{,\xi}^{bu} - \boldsymbol{E}_2^{uu}\boldsymbol{U}^{bu} = -\xi\boldsymbol{F}^{tu} - \xi^2\boldsymbol{F}^{bu} - \boldsymbol{F}^{suu} \tag{51}$$

$$\xi\boldsymbol{F}^{tc} = -\xi^2\boldsymbol{F}^{bc} - \boldsymbol{F}^{suc} - \boldsymbol{F}^{scc} \tag{52}$$

where $\boldsymbol{F}^{bu}$ and $\boldsymbol{F}^{bc}$ results directly from the partition of the known vector $\boldsymbol{F}^b = \{\boldsymbol{F}^{bu} \quad \boldsymbol{F}^{bc}\}^T$ and the vectors $\boldsymbol{F}^{suu}$, $\boldsymbol{F}^{scc}$ and $\boldsymbol{F}^{suc}$ are defined by

$$\boldsymbol{F}^{suu} = \xi^2 \boldsymbol{E}_0^{uc} \boldsymbol{U}_{,\xi\xi}^{bc} + \xi(\boldsymbol{E}_0^{uc} + (\boldsymbol{E}_1^{cu})^T - \boldsymbol{E}_1^{uc})\boldsymbol{U}_{,\xi}^{bc} - \boldsymbol{E}_2^{uc}\boldsymbol{U}^{bc} \tag{53}$$

$$\boldsymbol{F}^{scc} = \xi^2 \boldsymbol{E}_0^{cc} \boldsymbol{U}_{,\xi\xi}^{bc} + \xi\left[\boldsymbol{E}_0^{cc} + (\boldsymbol{E}_1^{cc})^T - \boldsymbol{E}_1^{cc}\right]\boldsymbol{U}_{,\xi}^{bc} - \boldsymbol{E}_2^{cc}\boldsymbol{U}^{bc} \tag{54}$$

$$\boldsymbol{F}^{suc} = \xi^2 (\boldsymbol{E}_0^{uc})^T \boldsymbol{U}_{,\xi\xi}^{bu} + \xi\left[(\boldsymbol{E}_0^{uc})^T + (\boldsymbol{E}_1^{uc})^T - \boldsymbol{E}_1^{cu}\right]\boldsymbol{U}_{,\xi}^{bu} - (\boldsymbol{E}_2^{uc})^T\boldsymbol{U}^{bu} \tag{55}$$

in which $\boldsymbol{E}_i^{uu}, \boldsymbol{E}_i^{uc}, \boldsymbol{E}_i^{cu}, \boldsymbol{E}_i^{cc}$ for $i = 0,1,2$ are sub-matrices resulting from the partition of the matrix $\boldsymbol{E}_i$. Note that both $\boldsymbol{F}^{suu}$ and $\boldsymbol{F}^{scc}$ are known vectors obtained from the prescribed state variable on the side face whereas $\boldsymbol{F}^{suc}$ is given in terms of the unknown vector $\boldsymbol{U}^{hu}$. By following the same procedure, the relation (50) can be also partitioned into

$$\boldsymbol{Q}^{hu}(\xi) = \xi \boldsymbol{E}_0^{uu} \boldsymbol{U}_{,\xi}^{hu} + (\boldsymbol{E}_1^{uu})^T \boldsymbol{U}^{hu} + \boldsymbol{Q}^{huc}(\xi) \tag{56}$$

$$\boldsymbol{Q}^{hc}(\xi) = \xi (\boldsymbol{E}_0^{uc})^T \boldsymbol{U}_{,\xi}^{hu} + (\boldsymbol{E}_1^{uc})^T \boldsymbol{U}^{hu} + \boldsymbol{Q}^{hcc}(\xi) \tag{57}$$

where $\boldsymbol{Q}^{huc}(\xi)$ and $\boldsymbol{Q}^{hcc}(\xi)$ are known vectors defined by

$$\boldsymbol{Q}^{huc}(\xi) = \xi \boldsymbol{E}_0^{uc} \boldsymbol{U}_{,\xi}^{hc} + (\boldsymbol{E}_1^{cu})^T \boldsymbol{U}^{hc}, \qquad \boldsymbol{Q}^{hcc}(\xi) = \xi \boldsymbol{E}_0^{cc} \boldsymbol{U}_{,\xi}^{hc} + (\boldsymbol{E}_1^{cc})^T \boldsymbol{U}^{hc} \tag{58}$$

Now, a system of differential equations (51) together with the following two boundary conditions on the inner and outer boundaries (i.e., $\boldsymbol{Q}^{hu}(\xi_1) = -\boldsymbol{P}_1^u$ and $\boldsymbol{Q}^{hu}(\xi_2) = \boldsymbol{P}_2^u$) is sufficient for determining the general solution $\boldsymbol{U}^{hu}$ of the given boundary value problem. Note that $\boldsymbol{P}_1^u$ and $\boldsymbol{P}_2^u$ are vectors resulting from the partition of the vectors $\boldsymbol{P}_1$ and $\boldsymbol{P}_2$, respectively (i.e., $\boldsymbol{P}_1 = \{\boldsymbol{P}_1^u \quad \boldsymbol{P}_1^c\}^T$ and $\boldsymbol{P}_2 = \{\boldsymbol{P}_2^u \quad \boldsymbol{P}_2^c\}^T$). Once $\boldsymbol{U}^{hu}$ is determined, the vectors $\boldsymbol{F}^{hc}$, $\boldsymbol{P}_1^c$, and $\boldsymbol{P}_2^c$ can be readily obtained.

3. Solution Procedure

This section presents the procedure for obtaining the analytical solution of a system of linear, second-order, nonhomogeneous, ordinary differential equations (51) along with the prescribed conditions on both inner and outer boundaries. A corresponding eigenvalue problem is solved first to determine the homogeneous solution and the method of undetermined coefficients is then utilized to construct the particular solution associated with the distributed body source and the prescribed conditions on the side faces. Once the general solution is obtained, the boundary conditions on both inner and outer boundaries are enforced to determine all involved constants. Finally, the post-process for field quantities of interest such as the state variable and body flux is briefly described.

3.1. Determination of Homogeneous Solution

Following the standard procedure in the theory of differential equations, a homogeneous solution of a system of linear, second-order, Euler-Cauchy differential equations (51), denoted by $\boldsymbol{U}_0^{hu}$, takes the following form

$$\boldsymbol{U}_0^{hu}(\xi) = \sum_{i=1}^{2(m-p)\Lambda} c_i \xi^{\lambda_i} \boldsymbol{\psi}_i^u \tag{59}$$

where λ_i is termed the modal scaling factor, $\boldsymbol{\psi}_i$ is the $(m-p)\Lambda$-component vector representing the i^{th} mode of the state variable, and c_i are arbitrary constants denoting the contribution of the i^{th} mode. The nodal internal flux $\boldsymbol{Q}_0^{hu}(\xi)$ associated with $\boldsymbol{U}_0^{hu}$ can be obtained as

$$\boldsymbol{Q}_0^{hu}(\xi) = \sum_{i=1}^{2(m-p)\Lambda} c_i \xi^{\lambda_i} \left[\lambda_i \boldsymbol{E}_0^{uu} + (\boldsymbol{E}_1^{uu})^T \right] \boldsymbol{\psi}_i^u = \sum_{i=1}^{2(m-p)\Lambda} c_i \xi^{\lambda_i} \boldsymbol{q}_i^u \tag{60}$$

where $\boldsymbol{q}_i^u$ is termed the i^{th} modal internal flux defined in terms of $\boldsymbol{\psi}_i^u$ by

$$\boldsymbol{q}_i^u = \left[\lambda_i \boldsymbol{E}_0^{uu} + (\boldsymbol{E}_1^{uu})^T \right] \boldsymbol{\psi}_i^u \tag{61}$$

By substituting (59) into (51) and then employing arbitrariness of c_i, it results in

$$\left\{\lambda_i^2 \boldsymbol{E}_0^{uu} + \lambda_i \left[(\boldsymbol{E}_1^{uu})^T - \boldsymbol{E}_1^{uu}\right] - \boldsymbol{E}_2^{uu}\right\} \boldsymbol{\psi}_i^u = \boldsymbol{0} \quad \forall i \in \{1,2,...,2(m-p)\Lambda\} \tag{62}$$

By further rearranging terms in (61) such that

$$\lambda_i \boldsymbol{\psi}_i^u = -(\boldsymbol{E}_0^{uu})^{-1} (\boldsymbol{E}_1^{uu})^T \boldsymbol{\psi}_i^u + (\boldsymbol{E}_0^{uu})^{-1} \boldsymbol{q}_i^u \tag{63}$$

where $(\boldsymbol{E}_0^{uu})^{-1}$ denotes the inverse of $\boldsymbol{E}_0^{uu}$, and then substituting this result into (62), it finally yields

$$\lambda_i \boldsymbol{q}_i^u = \left[\boldsymbol{E}_2^{uu} - \boldsymbol{E}_1^{uu} (\boldsymbol{E}_0^{uu})^{-1} (\boldsymbol{E}_1^{uu})^T\right] \boldsymbol{\psi}_i^u + \boldsymbol{E}_1^{uu} (\boldsymbol{E}_0^{uu})^{-1} \boldsymbol{q}_i^u \tag{64}$$

Now, by introducing a $2(m-p)\Lambda$-component vector $\boldsymbol{X}_i$ such that $\boldsymbol{X}_i = \{\boldsymbol{\psi}_i^u \quad \boldsymbol{q}_i^u\}^T$, equations (63) and (64) can be combined into a system of linear algebraic equations

$$\boldsymbol{A}\boldsymbol{X}_i = \lambda_i \boldsymbol{X}_i \tag{65}$$

where a coefficient matrix $\boldsymbol{A}$ is given by

$$\boldsymbol{A} = \begin{bmatrix} -(\boldsymbol{E}_0^{uu})^{-1} (\boldsymbol{E}_1^{uu})^T & (\boldsymbol{E}_0^{uu})^{-1} \\ \boldsymbol{E}_2^{uu} - \boldsymbol{E}_1^{uu} (\boldsymbol{E}_0^{uu})^{-1} (\boldsymbol{E}_1^{uu})^T & \boldsymbol{E}_1^{uu} (\boldsymbol{E}_0^{uu})^{-1} \end{bmatrix} \tag{66}$$

Determination of $2(m-p)\Lambda$ pairs of $\{\lambda_i, \boldsymbol{X}_i\}$ can be achieved by solving the eigenvalue problem (65) where λ_i denotes the eigenvalue and $\boldsymbol{X}_i$ are the associated eigenvector. It should be remarked that since $\boldsymbol{A}$ is, in general, not symmetric, $\{\lambda_i, \boldsymbol{X}_i\}$ involves complex numbers. In fact, only a half of the eigenvalues has the positive real part whereas the other half has the negative real part. Let $\boldsymbol{\lambda}^+$ and $\boldsymbol{\lambda}^-$ be $(m-p)\Lambda \times (m-p)\Lambda$ diagonal matrices containing eigenvalues with the positive and negative real parts, respectively, $\boldsymbol{\Phi}^{\psi+}$ and $\boldsymbol{\Phi}^{q+}$ be matrices whose columns are $\boldsymbol{\psi}_i^u$ and $\boldsymbol{q}_i^u$ of the eigenvector $\boldsymbol{X}_i = \{\boldsymbol{\psi}_i^u \quad \boldsymbol{q}_i^u\}^T$ associated with λ_i in $\boldsymbol{\lambda}^+$, and $\boldsymbol{\Phi}^{\psi-}$ and $\boldsymbol{\Phi}^{q-}$ be matrices whose columns are $\boldsymbol{\psi}_i^u$ and $\boldsymbol{q}_i^u$ of the eigenvector $\boldsymbol{X}_i = \{\boldsymbol{\psi}_i^u \quad \boldsymbol{q}_i^u\}^T$ associated with λ_i in $\boldsymbol{\lambda}^-$. Now, the homogeneous solutions $\boldsymbol{U}_0^{hu}$ and $\boldsymbol{Q}_0^{hu}(\xi)$ are given by

$$\boldsymbol{U}_0^{hu}(\xi) = \boldsymbol{\Phi}^{\psi+} \boldsymbol{\Pi}^+(\xi) \boldsymbol{C}^+ + \boldsymbol{\Phi}^{\psi-} \boldsymbol{\Pi}^-(\xi) \boldsymbol{C}^- \tag{67}$$

$$\boldsymbol{Q}_0^{hu}(\xi) = \boldsymbol{\Phi}^{q+} \boldsymbol{\Pi}^+(\xi) \boldsymbol{C}^+ + \boldsymbol{\Phi}^{q-} \boldsymbol{\Pi}^-(\xi) \boldsymbol{C}^- \tag{68}$$

where $\boldsymbol{\Pi}^+$ and $\boldsymbol{\Pi}^-$ are diagonal matrices obtained by replacing the diagonal entries λ_i of the matrices $\boldsymbol{\lambda}^+$ and $\boldsymbol{\lambda}^-$ by a function ξ^{λ_i}, respectively; and $\boldsymbol{C}^+$ and $\boldsymbol{C}^-$ are vectors containing arbitrary constants representing the contribution of each mode. It is apparent that the diagonal entries of $\boldsymbol{\Pi}^+$ become infinite when $\xi \to \infty$ whereas those of $\boldsymbol{\Pi}^-$ is unbounded when $\xi \to 0$. As a result, $\boldsymbol{C}^+$ is taken to be $\boldsymbol{0}$ to ensure the boundedness of the solution for unbounded bodies and, similarly, the condition $\boldsymbol{C}^- = \boldsymbol{0}$ is enforced for bodies containing the scaling center.

3.2. Determination of Particular Solution

In the present study, the distributed body source $\boldsymbol{b}$, the prescribed surface flux $\boldsymbol{t}_1^s$ on the side-face-1, the prescribed surface flux $\boldsymbol{t}_2^s$ on the side-face-2, and the prescribed state variable $\boldsymbol{U}^{hc}$ on the side faces are assumed to admit the form

DOI:10.4186/ej.2017.21.7.333

$$\boldsymbol{b}(\xi,s)=\sum_{\kappa_j\in\mathbb{R}^*}\xi^{\kappa_j}\bar{\boldsymbol{b}}_j(s),\boldsymbol{t}_1^s(\xi)=\sum_{\tau_j\in\mathbb{R}^*}\xi^{\tau_j}\bar{\boldsymbol{t}}_j^{s1},\ \boldsymbol{t}_2^s(\xi)=\sum_{\gamma_j\in\mathbb{R}^*}\xi^{\gamma_j}\bar{\boldsymbol{t}}_j^{s2},\ \boldsymbol{U}^{bc}(\xi)=\sum_{\omega_j\in\mathbb{R}^*}\xi^{\omega_j}\bar{\boldsymbol{U}}_j^{bc} \tag{69}$$

where $\mathbb{R}^*$ denotes a set of non-negative real numbers, $\bar{\boldsymbol{b}}_j(s)$ are given vector-value functions, and $\bar{\boldsymbol{t}}_j^{s1}$, $\bar{\boldsymbol{t}}_j^{s2}$, $\bar{\boldsymbol{U}}_j^{bc}$ are given constant vectors. Substituting (69) into (43), (45) and (53) yields

$$\boldsymbol{F}^b=\sum_{\kappa_j\in\mathbb{R}^*}\xi^{\kappa_j}\bar{\boldsymbol{F}}_j^b,\quad \boldsymbol{F}_1^t=\sum_{\tau_j\in\mathbb{R}^*}\xi^{\tau_j}\bar{\boldsymbol{F}}_j^{t1},\quad \boldsymbol{F}_2^t=\sum_{\gamma_j\in\mathbb{R}^*}\xi^{\gamma_j}\bar{\boldsymbol{F}}_j^{t2},\quad \boldsymbol{F}^{suu}=\sum_{\omega_j\in\mathbb{R}^*}\xi^{\omega_j}\bar{\boldsymbol{F}}_j^{suu} \tag{70}$$

where $\bar{\boldsymbol{F}}_j^b$, $\bar{\boldsymbol{F}}_j^{t1}$, $\bar{\boldsymbol{F}}_j^{t2}$, and $\bar{\boldsymbol{F}}_j^{suu}$ are constant vectors defined, in terms of prescribed data, by

$$\bar{\boldsymbol{F}}_j^b=\left\{\int_{s_1}^{s_2}\phi_{(1)}\bar{\boldsymbol{b}}_j(s)J^b ds\quad \int_{s_1}^{s_2}\phi_{(2)}\bar{\boldsymbol{b}}_j(s)J^b ds\quad\cdots\quad \int_{s_1}^{s_2}\phi_{(m)}\bar{\boldsymbol{b}}_j(s)J^b ds\right\}^T \tag{71}$$

$$\bar{\boldsymbol{F}}_j^{t1}=\{J_1^{\xi b}\bar{\boldsymbol{t}}_j^{s1}\quad \boldsymbol{0}\quad\cdots\quad \boldsymbol{0}\},\ \bar{\boldsymbol{F}}_j^{t2}=\{\boldsymbol{0}\quad \boldsymbol{0}\quad\cdots\quad J_2^{\xi b}\bar{\boldsymbol{t}}_j^{s2}\}^T \tag{72}$$

$$\bar{\boldsymbol{F}}_j^{suu}=\left\{\omega_j(\omega_j-1)\boldsymbol{E}_0^{uc}+\omega_j(\boldsymbol{E}_0^{uc}+(\boldsymbol{E}_1^{cu})^T-\boldsymbol{E}_1^{uc})-\boldsymbol{E}_2^{uc}\right\}\bar{\boldsymbol{U}}_j^{bc} \tag{73}$$

Based on this form of prescribed data and the method of undetermined coefficients, the particular solution of (51), denoted by $\boldsymbol{U}_1^{bu}$, takes the form

$$\boldsymbol{U}_1^{bu}(\xi)=\boldsymbol{U}_1^{bub}(\xi)+\boldsymbol{U}_1^{but1}(\xi)+\boldsymbol{U}_1^{but2}(\xi)+\boldsymbol{U}_1^{buu}(\xi) \tag{74}$$

where

$$\boldsymbol{U}_1^{bub}(\xi)=\sum_{\kappa_j\in\mathbb{R}^*}\xi^{\kappa_j+2}\boldsymbol{c}_j^b,\quad \boldsymbol{U}_1^{but1}(\xi)=\sum_{\tau_j\in\mathbb{R}^*}\xi^{\tau_j+1}\boldsymbol{c}_j^{t1},\quad \boldsymbol{U}_1^{but2}(\xi)=\sum_{\gamma_j\in\mathbb{R}^*}\xi^{\gamma_j+1}\boldsymbol{c}_j^{t2},\quad \boldsymbol{U}_1^{buu}(\xi)=\sum_{\omega_j\in\mathbb{R}^*}\xi^{\omega_j}\boldsymbol{c}_j^{uc} \tag{75}$$

with $\boldsymbol{c}_j^b$, $\boldsymbol{c}_j^{t1}$, $\boldsymbol{c}_j^{t2}$, and $\boldsymbol{c}_j^{uc}$ being vectors of unknown constants determined from the following four systems of linear algebraic equations

$$\left\{(\kappa_j+2)(\kappa_j+1)\boldsymbol{E}_0^{uu}+(\kappa_j+2)\left[\boldsymbol{E}_0^{uu}+(\boldsymbol{E}_1^{uu})^T-\boldsymbol{E}_1^{uu}\right]-\boldsymbol{E}_2^{uu}\right\}\boldsymbol{c}_j^b+\bar{\boldsymbol{F}}_j^{bu}=\boldsymbol{0} \tag{76}$$

$$\left\{(\tau_j+1)\tau_j\boldsymbol{E}_0^{uu}+(\tau_j+1)\left[\boldsymbol{E}_0^{uu}+(\boldsymbol{E}_1^{uu})^T-\boldsymbol{E}_1^{uu}\right]-\boldsymbol{E}_2^{uu}\right\}\boldsymbol{c}_j^{t1}+\bar{\boldsymbol{F}}_j^{tu1}=\boldsymbol{0} \tag{77}$$

$$\left\{(\gamma_j+1)\gamma_j\boldsymbol{E}_0^{uu}+(\gamma_j+1)\left[\boldsymbol{E}_0^{uu}+(\boldsymbol{E}_1^{uu})^T-\boldsymbol{E}_1^{uu}\right]-\boldsymbol{E}_2^{uu}\right\}\boldsymbol{c}_j^{t2}+\bar{\boldsymbol{F}}_j^{tu2}=\boldsymbol{0} \tag{78}$$

$$\left\{\omega_j(\omega_j-1)\boldsymbol{E}_0^{uu}+(\omega_j-1)\left[\boldsymbol{E}_0^{uu}+(\boldsymbol{E}_1^{uu})^T-\boldsymbol{E}_1^{uu}\right]-\boldsymbol{E}_2^{uu}\right\}\boldsymbol{c}_j^{uc}+\bar{\boldsymbol{F}}_j^{suu}=\boldsymbol{0} \tag{79}$$

where $\bar{\boldsymbol{F}}_j^{bu}$, $\bar{\boldsymbol{F}}_j^{tu1}$ and $\bar{\boldsymbol{F}}_j^{tu2}$ result from the following partitions $\bar{\boldsymbol{F}}_j^b=\{\bar{\boldsymbol{F}}_j^{bu}\quad \bar{\boldsymbol{F}}_j^{bc}\}^T$, $\bar{\boldsymbol{F}}_j^{t1}=\{\bar{\boldsymbol{F}}_j^{tu1}\quad \bar{\boldsymbol{F}}_j^{tc1}\}^T$, and $\bar{\boldsymbol{F}}_j^{t2}=\{\bar{\boldsymbol{F}}_j^{tu2}\quad \bar{\boldsymbol{F}}_j^{tc2}\}^T$, respectively. Once the particular solution $\boldsymbol{U}_1^{bu}(\xi)$ is obtained, the corresponding particular nodal internal flux, denoted by $\boldsymbol{Q}_1^{bu}(\xi)$, is calculated from

$$\boldsymbol{Q}_1^{bu}(\xi)=\xi\boldsymbol{E}_0^{uu}\boldsymbol{U}_{1,\xi}^{bu}+(\boldsymbol{E}_1^{uu})^T\boldsymbol{U}_1^{bu} \tag{80}$$

3.3. Final General Solution

The general solution $\boldsymbol{U}^{bu}(\xi)$ of (51) and the corresponding nodal internal flux $\boldsymbol{Q}^{bu}(\xi)$ are given by

$$\boldsymbol{U}^{hu}(\xi)=\boldsymbol{U}_0^{hu}(\xi)+\boldsymbol{U}_1^{hu}(\xi)=\boldsymbol{\Phi}^{\psi+}\boldsymbol{\Pi}^{+}(\xi)\boldsymbol{C}^{+}+\boldsymbol{\Phi}^{\psi-}\boldsymbol{\Pi}^{-}(\xi)\boldsymbol{C}^{-}+\boldsymbol{U}_1^{hu}(\xi) \tag{81}$$

$$\boldsymbol{Q}^{hu}(\xi)=\boldsymbol{Q}_0^{hu}(\xi)+\boldsymbol{Q}_1^{hu}(\xi)=\boldsymbol{\Phi}^{q+}\boldsymbol{\Pi}^{+}(\xi)\boldsymbol{C}^{+}+\boldsymbol{\Phi}^{q-}\boldsymbol{\Pi}^{-}(\xi)\boldsymbol{C}^{-}+\boldsymbol{Q}_1^{hu}(\xi) \tag{82}$$

By enforcing conditions on both inner and outer boundaries (i.e., $\boldsymbol{Q}^{hu}(\xi_1)=-\boldsymbol{P}_1^{u}$, $\boldsymbol{Q}^{hu}(\xi_2)=\boldsymbol{P}_2^{u}$), it leads to a systems of linear equations governing all constants contained in $\boldsymbol{C}^{+}$ and $\boldsymbol{C}^{-}$:

$$\begin{bmatrix}\boldsymbol{\Phi}^{q+}\boldsymbol{\Pi}^{+}(\xi_1) & \boldsymbol{\Phi}^{q-}\boldsymbol{\Pi}^{-}(\xi_1)\\ \boldsymbol{\Phi}^{q+}\boldsymbol{\Pi}^{+}(\xi_2) & \boldsymbol{\Phi}^{q-}\boldsymbol{\Pi}^{-}(\xi_2)\end{bmatrix}\begin{Bmatrix}\boldsymbol{C}^{+}\\ \boldsymbol{C}^{-}\end{Bmatrix}=\begin{Bmatrix}-\boldsymbol{P}_1^{u}\\ \boldsymbol{P}_2^{u}\end{Bmatrix}-\begin{Bmatrix}\boldsymbol{Q}_1^{hu}(\xi_1)\\ \boldsymbol{Q}_1^{hu}(\xi_2)\end{Bmatrix} \tag{83}$$

The system (83) can be, in principle, inverted to obtain

$$\begin{Bmatrix}\boldsymbol{C}^{+}\\ \boldsymbol{C}^{-}\end{Bmatrix}=\begin{bmatrix}\boldsymbol{\Phi}^{q+}\boldsymbol{\Pi}^{+}(\xi_1) & \boldsymbol{\Phi}^{q-}\boldsymbol{\Pi}^{-}(\xi_1)\\ \boldsymbol{\Phi}^{q+}\boldsymbol{\Pi}^{+}(\xi_2) & \boldsymbol{\Phi}^{q-}\boldsymbol{\Pi}^{-}(\xi_2)\end{bmatrix}^{-1}\left(\begin{Bmatrix}-\boldsymbol{P}_1^{u}\\ \boldsymbol{P}_2^{u}\end{Bmatrix}-\begin{Bmatrix}\boldsymbol{Q}_1^{hu}(\xi_1)\\ \boldsymbol{Q}_1^{hu}(\xi_2)\end{Bmatrix}\right) \tag{84}$$

By first applying (81) to obtain $\boldsymbol{U}^{hu}$ at $\xi=\xi_1$ and $\xi=\xi_2$, and then using the relation (84), it leads to

$$\boldsymbol{K}\begin{Bmatrix}\boldsymbol{U}^{hu}(\xi_1)\\ \boldsymbol{U}^{hu}(\xi_2)\end{Bmatrix}=\begin{Bmatrix}-\boldsymbol{P}_1^{u}\\ \boldsymbol{P}_2^{u}\end{Bmatrix}+\boldsymbol{K}\begin{Bmatrix}\boldsymbol{U}_1^{hu}(\xi_1)\\ \boldsymbol{U}_1^{hu}(\xi_2)\end{Bmatrix}-\begin{Bmatrix}\boldsymbol{Q}_1^{hu}(\xi_1)\\ \boldsymbol{Q}_1^{hu}(\xi_2)\end{Bmatrix} \tag{85}$$

where the coefficient matrix $\boldsymbol{K}$, commonly termed the stiffness matrix, is given by

$$\boldsymbol{K}=\begin{bmatrix}\boldsymbol{\Phi}^{q+}\boldsymbol{\Pi}^{+}(\xi_1) & \boldsymbol{\Phi}^{q-}\boldsymbol{\Pi}^{-}(\xi_1)\\ \boldsymbol{\Phi}^{q+}\boldsymbol{\Pi}^{+}(\xi_2) & \boldsymbol{\Phi}^{q-}\boldsymbol{\Pi}^{-}(\xi_2)\end{bmatrix}\begin{bmatrix}\boldsymbol{\Phi}^{\psi+}\boldsymbol{\Pi}^{+}(\xi_1) & \boldsymbol{\Phi}^{\psi-}\boldsymbol{\Pi}^{-}(\xi_1)\\ \boldsymbol{\Phi}^{\psi+}\boldsymbol{\Pi}^{+}(\xi_2) & \boldsymbol{\Phi}^{\psi-}\boldsymbol{\Pi}^{-}(\xi_2)\end{bmatrix}^{-1} \tag{86}$$

By enforcing the prescribed surface flux and the state variable on both inner and outer boundaries, a system of linear algebraic equations (85) is sufficient for determining all unknowns contained in the vectors $\{\boldsymbol{U}^{hu}(\xi_1)\quad \boldsymbol{U}^{hu}(\xi_2)\}^{T}$ and $\{-\boldsymbol{P}_1^{u}\quad \boldsymbol{P}_2^{u}\}^{T}$. Once the unknowns on both inner and outer boundaries are solved, the constant vectors $\boldsymbol{C}^{+}$ and $\boldsymbol{C}^{-}$ can be obtained from (84) and the general solution for both $\boldsymbol{U}^{hu}(\xi)$ and $\boldsymbol{Q}^{hu}(\xi)$ are obtained from (81) and (82), respectively.

3.4. Post-process for Field Quantities

Once the approximate general solution $\boldsymbol{U}^{hu}(\xi)$ is obtained, the approximate field quantities such as the state variable and the surface flux within the body can be determined. For instance, the approximate state variable at (ξ,s) can be obtained from

$$\boldsymbol{u}^{h}(\xi,s)=\boldsymbol{N}^{S}(s)\boldsymbol{U}^{h}(\xi)=\begin{bmatrix}\boldsymbol{N}^{Su}(s) & \boldsymbol{N}^{Sc}(s)\end{bmatrix}\begin{Bmatrix}\boldsymbol{U}^{hu}(\xi)\\ \boldsymbol{U}^{hc}(\xi)\end{Bmatrix}=\boldsymbol{N}^{Su}(s)\boldsymbol{U}^{hu}(\xi)+\boldsymbol{N}^{Sc}(s)\boldsymbol{U}^{hc}(\xi) \tag{87}$$

where $\boldsymbol{N}^{Su}$ and $\boldsymbol{N}^{Sc}$ are matrices resulting from the partition of $\boldsymbol{N}^{S}$. Similarly, the approximate body flux can be computed from

$$\boldsymbol{\sigma}^{h}(\xi,s)=\boldsymbol{D}\left[\boldsymbol{B}_1^{u}(s)\boldsymbol{U}_{,\xi}^{hu}(\xi)+\frac{1}{\xi}\boldsymbol{B}_2^{u}(s)\boldsymbol{U}^{hu}(\xi)\right]+\boldsymbol{D}\left[\boldsymbol{B}_1^{c}(s)\boldsymbol{U}_{,\xi}^{hc}(\xi)+\frac{1}{\xi}\boldsymbol{B}_2^{c}(s)\boldsymbol{U}^{hc}(\xi)\right] \tag{88}$$

where $\boldsymbol{B}_1^{u}$, $\boldsymbol{B}_1^{c}$ and $\boldsymbol{B}_2^{u}$, $\boldsymbol{B}_2^{c}$ are matrices resulting from the partition of the matrices $\boldsymbol{B}_1$ and $\boldsymbol{B}_2$, respectively. It is emphasized here again that the solutions (87) and (88) also apply to the special cases of

bounded and unbounded bodies. For bounded bodies containing the scaling center, $\boldsymbol{C}^{-}$ simply vanishes and, for unbounded bodies, $\boldsymbol{C}^{+}=\boldsymbol{0}$.

4. Numerical Results and Discussion

Numerical results of four representative problems are presented, in this section, to verify both the formulation and the implementation of the proposed technique. To demonstrate its capability to treat a variety of boundary value problems, general boundary conditions, and prescribed data on the side faces, three different types of problems associated with steady-state heat conduction ($\Lambda=1$), linear elasticity ($\Lambda=2$), and linear piezoelectricity ($\Lambda=3$), under various scenarios are considered. In the approximation, standard linear finite elements are employed to discretize both the defining curve and the trial and test functions. The accuracy and convergence of numerical solutions are confirmed by benchmarking with available analytical solutions and carrying out the analysis via a series of meshes.

4.1. Heat Conduction in Rectangular Domain

The proposed technique is first tested with a representative problem associated with the steady-state heat conduction ($\Lambda=1$). Let us consider a two-dimensional rectangular domain of dimensions l_1 and l_2 as shown schematically in Fig. 5(a). The domain is made of a medium with an isotropic heat conductivity k_0 (or, equivalently, $D_{11}=D_{22}=k_0, D_{12}=D_{21}=0$) and subjected to a uniform heat source $b_1=Q_0$. A zero temperature is prescribed along the boundary AD (i.e., $u_1^{AD}=0$) and a uniform surface heat flux q_0 is prescribed along the boundary BC (i.e., $t_1^{BC}=q_0$) whereas, along the boundaries AB and CD, the surface heat flux vanishes (i.e., $t_1^{AB}=t_1^{CD}=0$). For this particular case, the exact solution for the temperature field (i.e., $u_1(x)$) and body heat flux (i.e., $\sigma_{11}(x)$ and $\sigma_{21}(x)$) is given by

$$u_1=\frac{1}{k_0}\left[(q_0+Q_0 l_1)x_1-\frac{1}{2}Q_0 x_1^2\right] \tag{89}$$

$$\sigma_{11}=q_0+Q_0(l_1-x_1),\quad \sigma_{21}=0 \tag{90}$$

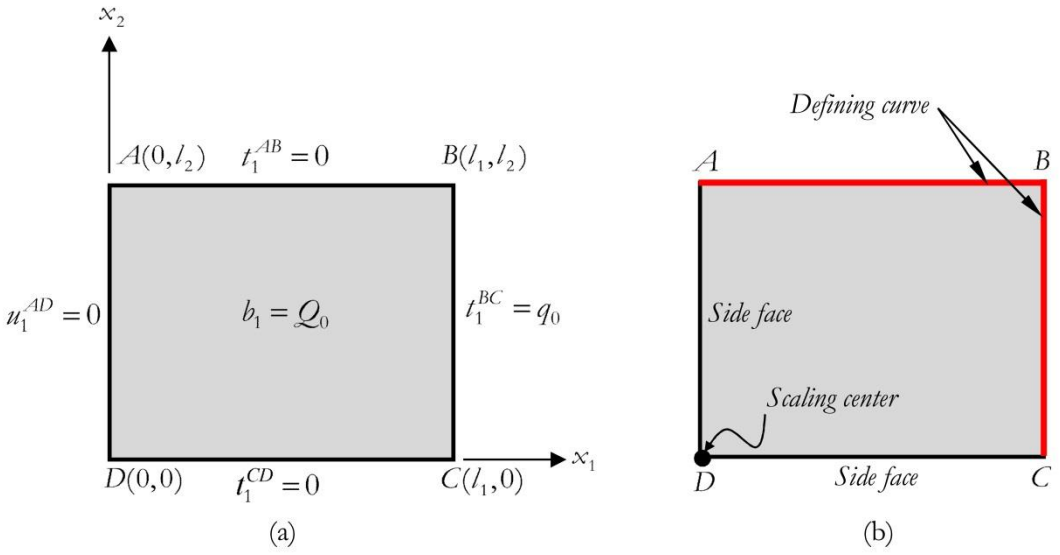

Fig. 5. Schematic of (a) rectangular domain under body heat source and mixed boundary conditions and (b) scaling center and defining curve used in scale boundary finite element analysis.

The domain geometry is described by the scaling center at point D and the defining curve ABC; as a result, the boundaries AD and CD become the side faces (see Figure 5(b)). In the numerical study, q_0 and Q_0 are chosen such that $Q_0 l_1 = 3q_0$ and the defining curve is discretized by a series of N identical linear elements. The normalized temperature $u_1 k_0 / q_0 l_1$ and the non-zero normalized body heat flux σ_{11}/q_0 along the boundary AB are reported in Table 1 for various values of normalized coordinate $\bar{x}_1 = x_1/l_1$ and meshes. Clearly, computed numerical solutions exhibit an excellent convergence behavior as the number of elements increases and, in addition, accurate results in comparison with the benchmark solution can be obtained even when few elements are employed to discretize the defining curve and solution along the boundary direction.

4.2. Linear Elastic Hollowed Cylinder under Uniform Pressure

Consider, next, a hollowed cylinder of the inner radius R_1 and outer radius R_2 (see Figure 6(a)). The cylinder is made of a homogeneous, linearly elastic, isotropic material with Young's modulus E and Poisson's ratio ν and is subjected to a plane-strain condition and uniform pressure p_1 and p_2 on the inner and outer boundaries, respectively, (i.e., $\Lambda = 2$ and the modulus matrix $\boldsymbol{D}$ with non-zero entries $D_{11} = D_{44} = (1-\nu)E/(1+\nu)(1-2\nu)$, $D_{14} = \nu E/(1+\nu)(1-2\nu)$, $D_{41} = \nu E/(1+\nu)(1-2\nu)$, $D_{22} = D_{23} = D_{32} = D_{33} = E/2(1+\nu)$). Due to the symmetry, it is sufficient to model this problem using only a quarter of the cylinder (see Figure 6(b)) with appropriate conditions on both side faces (i.e., the normal displacement and tangential traction on the side faces vanish). To describe the geometry, the scaling center is chosen at the center of the cylinder whereas the inner boundary is treated as the defining curve. In a numerical study, $R_2 / R_1 = 1.5$, $p_2 / p_1 = 2$, $\nu = 0.3$, and meshes with N identical linear elements are employed.

Results for the normalized radial displacement $(u_r/(p_1 R_1/E)$, normalized radial stress (σ_{rr}/p_1) and normalized hoop stress $(\sigma_{\theta\theta}/p_1)$ are reported along with existing analytical solutions [36] in Tables 2, 3 and 4, respectively, for four meshes (i.e., $N = 4, 8, 16, 32$). It is seen that numerical solutions generated by the proposed technique converge and exhibit excellent agreement with the benchmark solution. It is worth noting that the discretization with only few linear elements can capture numerical solution with sufficient accuracy.

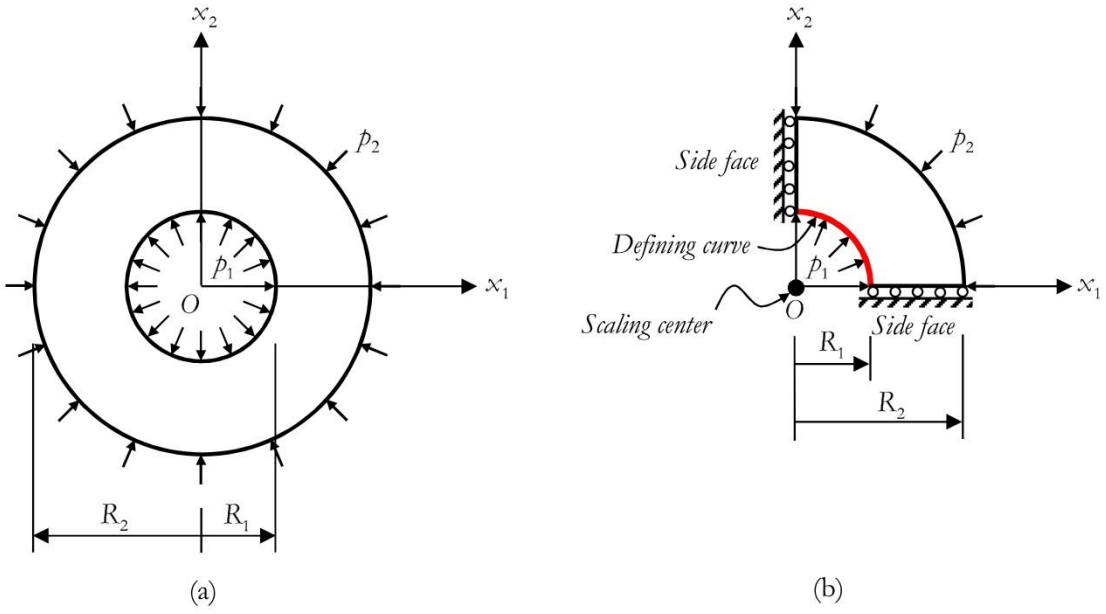

Fig. 6. Schematic of (a) hollowed cylinder under uniform internal and external pressure and (b) quarter of cylinder used in the analysis.

DOI:10.4186/ej.2017.21.7.333

Table 1. Normalized temperatures and body heat flux along the boundary *AB* of a rectangular domain subjected to body heat source and mixed boundary conditions.

$u_1 k_0 / q_0 l_1$						
$\bar{x}_1$	0.0	0.2	0.4	0.6	0.8	1.0
SBFEM, *N=4*	0.0000	0.7196	1.3287	1.8290	2.2175	2.4684
SBFEM, *N=8*	0.0000	0.7352	1.3520	1.8512	2.2332	2.4950
SBFEM, *N=16*	0.0000	0.7388	1.3580	1.8577	2.2382	2.4986
SBFEM, *N=32*	0.0000	0.7397	1.3595	1.8594	2.2395	2.4996
Exact solution	0.0000	0.7400	1.3600	1.8600	2.2400	2.5000
σ_{11} / q_0						
$\bar{x}_1$	0.0	0.2	0.4	0.6	0.8	1.0
SBFEM, *N=4*	3.8735	3.3211	2.7724	2.2297	1.6359	0.8099
SBFEM, *N=8*	3.9709	3.3802	2.7890	2.2037	1.6121	1.0222
SBFEM, *N=16*	3.9929	3.3950	2.7970	2.2005	1.6034	1.0006
SBFEM, *N=32*	3.9982	3.3988	2.7992	2.2001	1.6008	1.0000
Exact solution	4.0000	3.4000	2.8000	2.2000	1.6000	1.0000

Table 2. Normalized radial displacement of hollowed cylinder under internal and external uniform pressure. Results are reported at different values of radial coordinate $r = \sqrt{x_1^2 + x_2^2}$ for four meshes.

$u_r / (p_1 R_1 / E)$						
r / R_1	1.0	1.1	1.2	1.3	1.4	1.5
SBFEM, *N=4*	1.0958	0.9864	0.8943	0.8155	0.7473	0.6875
SBFEM, *N=8*	1.1124	1.0014	0.9080	0.8282	0.7590	0.6984
SBFEM, *N=16*	1.1166	1.0052	0.9115	0.8313	0.7619	0.7011
SBFEM, *N=32*	1.1177	1.0061	0.9123	0.8321	0.7627	0.7018
Exact solution	1.1180	1.0064	0.9126	0.8324	0.7629	0.7020

Table 3. Normalized radial stress of hollowed cylinder under internal and external uniform pressure. Results are reported at different values of radial coordinate $r = \sqrt{x_1^2 + x_2^2}$ for four meshes.

σ_{rr} / p_1						
r / R_1	1.0	1.1	1.2	1.3	1.4	1.5
SBFEM, *N=4*	-0.9821	-0.8289	-0.7124	-0.6217	-0.5497	-0.4917
SBFEM, *N=8*	-0.9955	-0.8401	-0.7218	-0.6298	-0.5568	-0.4979
SBFEM, *N=16*	-0.9989	-0.8429	-0.7242	-0.6319	-0.5586	-0.4995
SBFEM, *N=32*	-0.9997	-0.8436	-0.7248	-0.6324	-0.5590	-0.4999
Exact solution	-1.0000	-0.8438	-0.7250	-0.6325	-0.5592	-0.5000

Table 4. Normalized hoop stress of hollowed cylinder under internal and external uniform pressure. Results are reported at different values of radial coordinate $r = \sqrt{x_1^2 + x_2^2}$ for four meshes.

$\sigma_{\theta\theta} / p_1$						
r / R_1	1.0	1.1	1.2	1.3	1.4	1.5
SBFEM, *N=4*	0.7833	0.6301	0.5136	0.4229	0.3510	0.2929
SBFEM, *N=8*	0.7958	0.6404	0.5222	0.4301	0.3571	0.2982
SBFEM, *N=16*	0.7990	0.6429	0.5243	0.4319	0.3587	0.2996
SBFEM, *N=32*	0.7997	0.6436	0.5248	0.4324	0.3591	0.2999
Exact solution	0.8000	0.6438	0.5250	0.4325	0.3592	0.3000

DOI:10.4186/ej.2017.21.7.333

4.3. Linear Elastic Square Plate under Mixed Boundary Conditions

Another representative problem for linear elasticity ($\Lambda = 2$) is chosen to demonstrate the capability of the implemented procedure to treat problems with distributed body source and prescribed state variable and surface flux on the boundary. Consider a plane-strain, square plate $ABCD$ of dimension $l \times l$ and made of a homogeneous, isotropic, linearly elastic material of Young's modulus E and Poisson's ratio ν as shown schematically in Figure 7(a). Note that the modulus matrix $\boldsymbol{D}$ for this particular problem is the same as the previous case. The plate is subjected to a linear body force field $b_1 = 2b_0(1+\bar{x}_2)$, $b_2 = 2b_0(1-\bar{x}_1)$ with b_0 denoting a constant and $\bar{x}_1 = x_1/l$, $\bar{x}_2 = x_2/l$ denoting the normalized coordinates whereas the nonuniform traction and homogeneous displacement boundary conditions are prescribed on its four sides as follows:

Side AB: $t_1^{AB} = b_0 l(3+14\bar{x}_1 - \bar{x}_1^2)$ and $t_2^{AB} = 2b_0 l(-4+4\bar{x}_1 + 3\bar{x}_1^2)$
Side BC: $t_1^{BC} = 6b_0 l(\bar{x}_2^2 - 2)$ and $t_2^{BC} = b_0 l(1+14\bar{x}_2 + \bar{x}_2^2)$
Side AD: $u_1^{AD} = 0$ and $t_2^{AD} = -b_0 l(2\bar{x}_2 + \bar{x}_2^2)$
Side CD: $t_1^{CD} = b_0 l(\bar{x}_1^2 - 2\bar{x}_1)$ and $u_2^{CD} = 0$

The exact solution for this particular problem under the plane strain condition can be readily obtained from a classical theory of linear elasticity and final results are given by

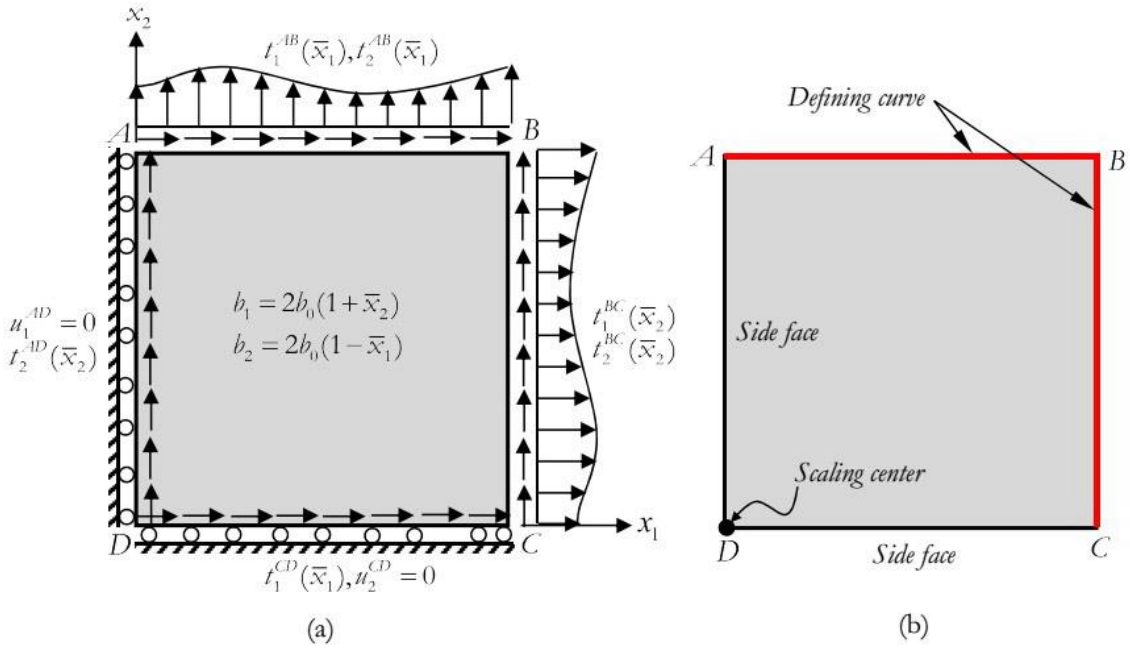

Fig 7. Schematic of (a) elastic square plate under mixed boundary conditions and (b) scaling center and defining curve used in scale boundary finite element analysis.

$$Eu_1^{exact} = -2b_0 l^2(1+\nu)(1+\bar{x}_1 - 2\bar{x}_2 + \bar{x}_1^2 - 3\bar{x}_2^2 + \bar{x}_1\bar{x}_2)\bar{x}_1 \tag{91}$$

$$Eu_2^{exact} = -2b_0 l^2(1+\nu)(-1-2\bar{x}_1 + \bar{x}_2 - 3\bar{x}_1^2 + \bar{x}_2^2 - \bar{x}_1\bar{x}_2)\bar{x}_2 \tag{92}$$

$$\sigma_{11}^{exact} = -\sigma_{22}^{exact} = -2b_0 l(1+2\bar{x}_1 - 2\bar{x}_2 + 3\bar{x}_1^2 - 3\bar{x}_2^2 + 2\bar{x}_1\bar{x}_2) \tag{93}$$

$$\sigma_{12}^{exact} = -b_0 l(-2\bar{x}_1 - 2\bar{x}_2 + \bar{x}_1^2 - \bar{x}_2^2 - 12\bar{x}_1\bar{x}_2) \tag{94}$$

The geometry of the plate is fully described by the scaling center at point D and the defining curve ABC and, as a result, the boundaries AD and CD become the side faces (see Figure 7(b)). In the analysis, Poisson's ration is taken as $\nu = 0.3$ and the defining curve is discretized by N identical linear elements. The

normalized displacements Eu_1/b_0l^2 and Eu_2/b_0l^2 along the boundaries *AB* and *BC* are reported in Tables 5 and 6 for various locations and meshes. It can be seen that numerical solutions converges to the exact solution as the number of elements *N* used to discretize the defining curve increases and, in addition, only few number of degrees of freedom is sufficient to obtain accurate displacements. The normalized normal stress components σ_{11}/b_0l and σ_{22}/b_0l along the boundaries *CD* and *AD* are also reported in Figures 8 and 9 along with the exact solution. Similar to the displacements, the proposed method also yields highly accurate stress components and the good convergent behavior; in particular, results obtained from all meshes are nearly indistinguishable from the benchmark solution.

Table 5. Normalized displacements along the boundary *AB* of elastic square plate subjected to mixed boundary conditions.

	Eu_1/b_0l^2					
$\bar{x}_1$	0.0	0.2	0.4	0.6	0.8	1.0
SBFEM, *N=8*	0.0000	1.8132	3.0677	3.6989	3.5973	2.6088
SBFEM, *N=16*	0.0000	1.8340	3.1482	3.7916	3.6349	2.6036
SBFEM, *N=32*	0.0000	1.8489	3.1558	3.7996	3.6578	2.6013
SBFEM, *N=64*	0.0000	1.8501	3.1608	3.8055	3.6592	2.6004
Exact solution	0.0000	1.8512	3.1616	3.8064	3.6608	2.6000
	Eu_2/b_0l^2					
$\bar{x}_1$	0.0	0.2	0.4	0.6	0.8	1.0
SBFEM, *N=8*	-2.7256	-0.7721	1.8011	4.9689	8.6766	12.8397
SBFEM, *N=16*	-2.6262	-0.7306	1.7661	4.8982	8.6579	12.9369
SBFEM, *N=32*	-2.6051	-0.7310	1.7700	4.8929	8.6363	12.9780
SBFEM, *N=64*	-2.6009	-0.7281	1.7679	4.8886	8.6333	13.0038
Exact solution	-2.6000	-0.7280	1.7680	4.8880	8.6320	13.0000

Table 6. Normalized displacements along the boundary *BC* of elastic square plate subjected to mixed boundary conditions.

	Eu_1/b_0l^2					
$\bar{x}_2$	0.0	0.2	0.4	0.6	0.8	1.0
SBFEM, *N=8*	-7.9407	-7.0248	-5.5067	-3.3831	-0.6694	2.6008
SBFEM, *N=16*	-7.8346	-6.9726	-5.5213	-3.4319	-0.7027	2.6012
SBFEM, *N=32*	-7.8086	-6.9716	-5.5119	-3.4297	-0.7246	2.6006
SBFEM, *N=64*	-7.8021	-6.9683	-5.5126	-3.4320	-0.7268	2.6143
Exact solution	-7.8000	-6.9680	-5.5120	-3.4320	-0.7280	2.6000
	Eu_2/b_0l^2					
$\bar{x}_2$	0.0	0.2	0.4	0.6	0.8	1.0
SBFEM, *N=8*	0.0000	3.0812	6.0130	8.7017	11.0266	12.8397
SBFEM, *N=16*	0.0000	3.0922	6.0621	8.7806	11.1096	12.9369
SBFEM, *N=32*	0.0000	3.0978	6.0699	8.7924	11.1408	12.9780
SBFEM, *N=64*	0.0000	3.0988	6.0729	8.7973	11.1465	13.0038
Exact solution	0.0000	3.0992	6.0736	8.7984	11.1488	13.0000

4.4. Linear Piezoelectric Square Plate

As a final example, a representative boundary value problem associated with the linear piezoelectricity ($\Lambda = 3$) is investigated to further highlight the capability of the proposed technique to treat linear multi-field problems. Let us consider a two-dimensional square plate of length l and made of a linear piezoelectric solid with all material constants taken from PZT-4 [5] as shown in Figure 10(a). In particular, all non-zero entries of the modulus matrix $\boldsymbol{D}$ are given explicitly by $D_{11} = 139\ GPa$, $D_{15} = D_{51} = 74.3\ GPa$,

$D_{16} = D_{61} = -6.98\ Cm^{-2}$, $D_{22} = D_{24} = D_{42} = D_{44} = 25.6\ GPa$, $D_{33} = 6.0 \times 10^{-9}\ C(Vm)^{-1}$, $D_{34} = D_{43} = 13.44\ Cm^{-2}$, $D_{55} = 113\ GPa$, $D_{56} = D_{65} = 13.84\ Cm^{-2}$, and $D_{66} = 5.47 \times 10^{-9}\ C(Vm)^{-1}$. For a purpose of verification, a set of prescribed data such as the distributed body source and boundary conditions on four sides is chosen such that the exact solution for the displacements (u_1 and u_2) and the electric potential (u_3) takes the following form

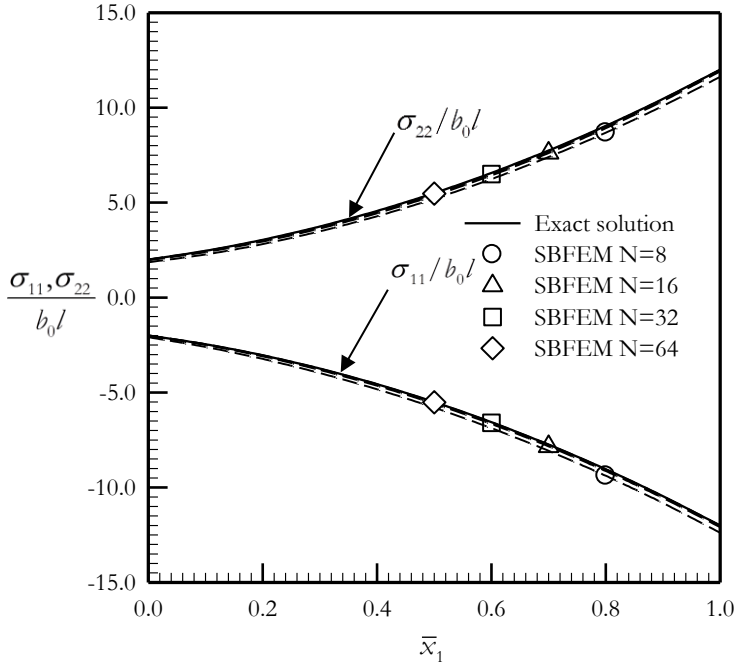

Fig. 8 Normalized normal stress components along the boundary *CD* of elastic square plate subjected to mixed boundary conditions.

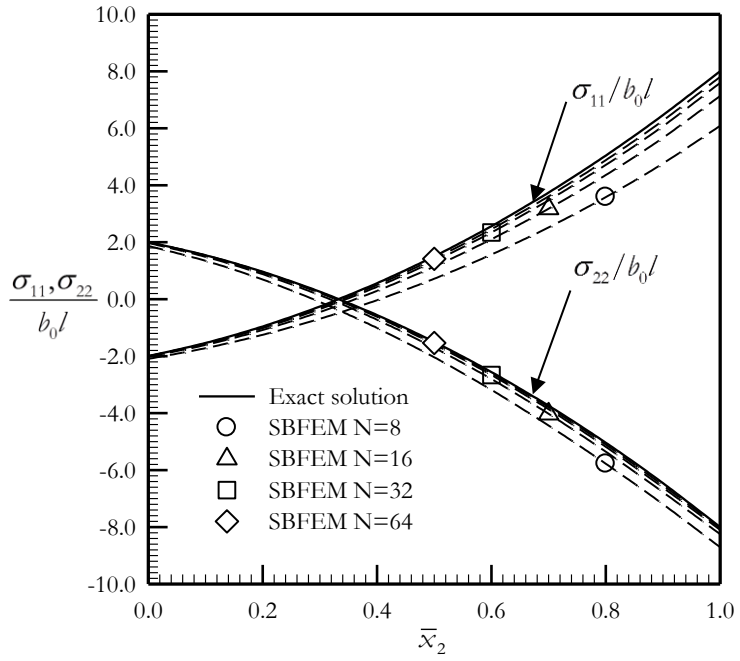

Fig. 9. Normalized normal stress components along the boundary *AD* of elastic square plate subjected to mixed boundary conditions.

DOI:10.4186/ej.2017.21.7.333

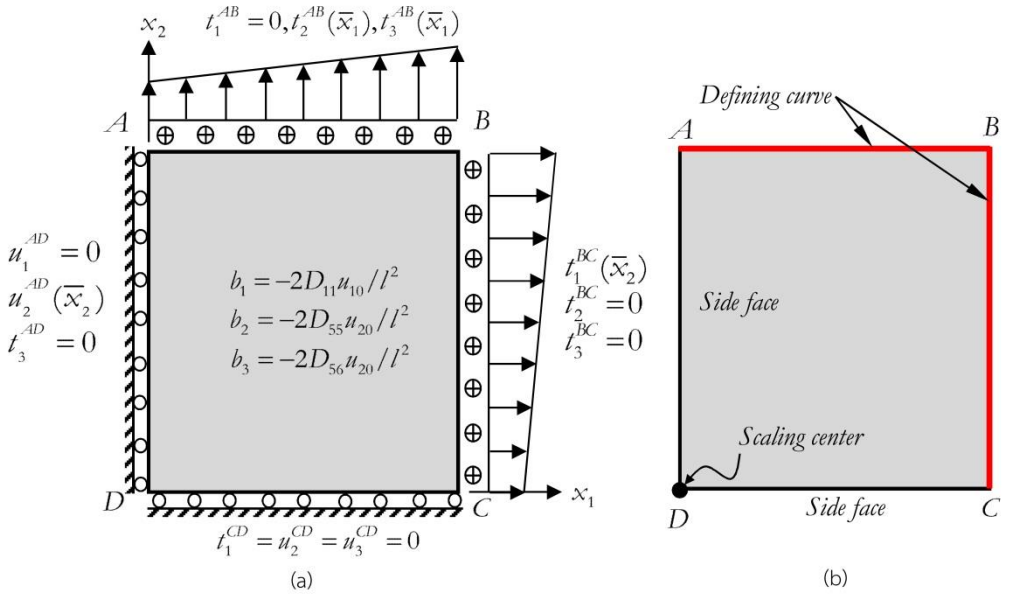

Fig. 10. Schematic of (a) linear piezoelectric square plate under mixed boundary conditions and (b) scaling center and defining curve used in scale boundary finite element analysis.

$$u_1 = u_{10}\bar{x}_1^2, \quad u_2 = u_{20}\bar{x}_2^2, \quad u_3 = \phi_0\bar{x}_2 \tag{95}$$

where u_{10} , u_{20} , ϕ_0 are given constants and $\bar{x}_1 = x_1/l$, $\bar{x}_2 = x_2/l$ are normalized coordinates. The corresponding exact stress field $(\sigma_{11},\sigma_{12},\sigma_{21},\sigma_{22})$ and electrical induction vector $(\sigma_{13},\sigma_{23})$ are given by

$$\sigma_{11} = (2D_{11}u_{10}\bar{x}_1 + 2D_{15}u_{20}\bar{x}_2 + D_{16}\phi_0)/l, \quad \sigma_{12} = \sigma_{21} = 0, \tag{96}$$

$$\sigma_{22} = (2D_{15}u_{10}\bar{x}_1 + 2D_{55}u_{20}\bar{x}_2 + D_{56}\phi_0)/l \tag{97}$$

$$\sigma_{13} = 0, \quad \sigma_{23} = (2D_{16}u_{10}\bar{x}_1 + 2D_{56}u_{20}\bar{x}_2 - D_{66}\phi_0)/l \tag{98}$$

The distributed body source that is in equilibrium with the above stress and electric induction can readily be obtained from (4) as

$$b_1 = -2D_{11}u_{10}/l^2, \quad b_2 = -2D_{55}u_{20}/l^2, \quad b_3 = -2D_{56}u_{20}/l^2 \tag{99}$$

In the modeling, the scaling center is chosen at a point *D* and the prescribed conditions on the side faces *AD* and *CD* and the boundaries *AB* and *BC* are given below

Side *AB*: $t_1^{AB}=0$, $t_2^{AB}=(2D_{15}u_{10}\bar{x}_1+2D_{55}u_{20}+D_{56}\phi_0)/l$, $t_3^{AB}=(2D_{16}u_{10}\bar{x}_1+2D_{56}\bar{u}_{20}-D_{66}\phi_0)/l$

Side *BC*: $t_1^{BC}=(2D_{11}u_{10}+2D_{15}u_{20}\bar{x}_2+D_{16}\phi_0)/l$, $t_2^{BC}=0$, $t_3^{BC}=0$

Side *AD*: $u_1^{AD}=0$, $u_2^{AD}=u_{20}\bar{x}_2^2$, $t_3^{AD}=0$

Side *CD*: $t_1^{CD}=0$, $u_2^{CD}=0$, $u_3^{CD}=0$

It is worth noting that the boundary conditions shown above are chosen to represent the general prescribed data on the side faces and boundaries of the domain. In the numerical study, a series of meshes with *N* identical linear elements is constructed to discretize the defining curve and solution along the scale boundary direction and $u_{20}/u_{10}=2$, $D_{16}\phi_0/D_{11}u_{10}=1$ are employed. Computed displacements and electric potential along the diagonal line *BD* are reported in Table 7 for various meshes. It is seen for this particular problem that the proposed technique yield highly accurate results even when relatively coarse meshes containing only few degrees of freedom are employed. In addition, the improvement of solutions as the

mesh is refined is clearly observed. The good quality of numerical solutions is also confirmed for the body flux as indicate in Figures 11 and 12. Computed stresses and electrical induction along the diagonal line *BD* show an excellent agreement with the exact solution; in particular, only slight difference between solutions can be seen for very coarse meshes while almost indistinguishable results are obtained for fine meshes.

Table 7. Normalized displacements and electrical potential along the diagonal line *BD* of linear piezoelectric square plate subjected to mixed boundary conditions. Results are reports as a function of normalized length $\bar{s} = s/\sqrt{2}l$ where s is the length along the line *BD* measured from point *D*.

			u_1/u_{10}			
$\bar{s}$	0.0	0.2	0.4	0.6	0.8	1.0
SBFEM, *N=4*	0.0000	0.0369	0.1351	0.3278	0.6291	1.0459
SBFEM, *N=8*	0.0000	0.0393	0.1531	0.3503	0.6360	1.0252
SBFEM, *N=16*	0.0000	0.0398	0.1582	0.3574	0.6385	1.0098
SBFEM, *N=32*	0.0000	0.0400	0.1596	0.3593	0.6396	1.0033
Exact solution	0.0000	0.0400	0.1600	0.3600	0.6400	1.0000
			u_2/u_{20}			
$\bar{s}$	0.0	0.2	0.4	0.6	0.8	1.0
SBFEM, *N=4*	0.0000	0.0821	0.3272	0.7222	1.2554	1.9134
SBFEM, *N=8*	0.0000	0.0803	0.3220	0.7213	1.2739	1.9679
SBFEM, *N=16*	0.0000	0.0801	0.3205	0.7204	1.2786	1.9891
SBFEM, *N=32*	0.0000	0.0800	0.3201	0.7201	1.2797	1.9965
Exact solution	0.0000	0.0800	0.3200	0.7200	1.2800	2.0000
			u_3/ϕ_0			
$\bar{s}$	0.0	0.2	0.4	0.6	0.8	1.0
SBFEM, *N=4*	0.0000	0.2013	0.4019	0.6013	0.7991	0.9938
SBFEM, *N=8*	0.0000	0.2003	0.4004	0.6003	0.7998	0.9976
SBFEM, *N=16*	0.0000	0.2001	0.4001	0.6001	0.7999	0.9992
SBFEM, *N=32*	0.0000	0.2000	0.4000	0.6000	0.8000	0.9997
Exact solution	0.0000	0.2000	0.4000	0.6000	0.8000	1.0000

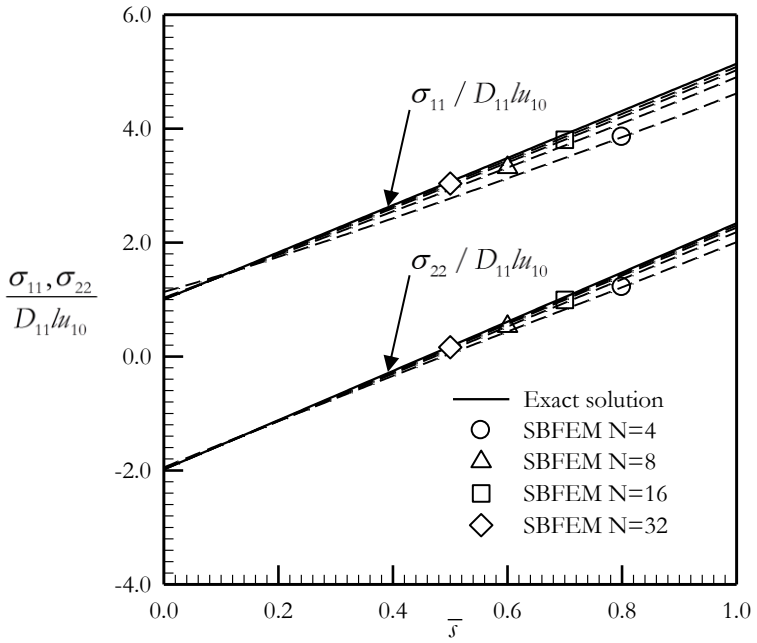

Fig. 11. Normalized non-zero stress components along the diagonal line *BD* of a piezoelectric square plate subjected to mixed boundary conditions. Results are reports as a function of normalized length $\bar{s} = s/\sqrt{2}l$ where s is the length along the line *BD* measured from point *D*.

DOI:10.4186/ej.2017.21.7.333

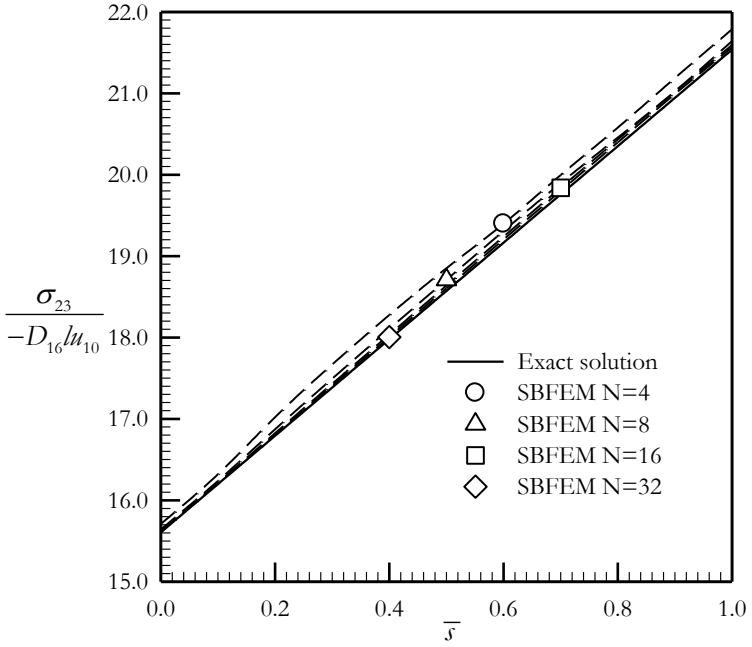

Fig. 12. Normalized a non-zero electrical induction component along the diagonal line *BD* of a piezoelectric square plate subjected to mixed boundary conditions. Results are reports as a function of normalized $\overline{s} = s/\sqrt{2}l$ where s is the length along the line *BD* measured from point *D*.

5. Conclusion and Remarks

A numerical technique based upon the scaled boundary finite element method (SFBEM) has been successfully developed for solving two-dimensional, multi-field boundary value problems. Both the formulation and implementations have been established in a general framework allowing various classes of linear boundary value problems (e.g., steady-state heat conduction problems, Laplace's equation, linear elasticity, linear piezoelectricity, etc.) and a set of general data such as the domain geometry, the prescribed distributed body source, the prescribed boundary conditions, and the contribution of the side-face conditions to be treated in a single, unified fashion. Results from an extensive numerical study for various scenarios have revealed that the proposed SBFEM yields highly accurate numerical solutions with the good convergence behavior. Relatively coarse meshes containing only few degrees of freedom have been found to accurately capture both the state variable and the body flux. In particular, both prescribed state variables and prescribed surface flux along the side faces and the general mixed boundary conditions along the scale boundary direction have been implemented into the proposed procedure and this, therefore, provides the flexibility in the selection of the scaling center and defining curve for describing the domain geometry.

Although the proposed technique has been implemented within the context of two-dimensional boundary value problems with domains described by a single scaling center, its underlying formulation and computational procedure are sufficiently general and should provide an essential basis for the extension to treat more general bodies such as those requiring multiple scaling centers to fully describe their geometry. Another potential extension is to generalize the present unified framework to three-dimensional multi-field problems.

Acknowledgements

The authors gratefully acknowledge the support provided by CU Scholarship for ASEAN Countries 2013 and Thailand Research Fund (Grant No. RSA5980032).

References

[1] J. P. Wolf and C. Song, "The scaled boundary finite-element method – A primer: derivations," *Computers & Structures*, vol. 78, pp. 191-210, 2000.

[2] J. P. Wolf and C. Song, "The scaled boundary finite-element method – A primer: Solution procedures," *Computers & Structures*, vol. 78, pp. 211-225, 2000.

[3] J. P. Wolf, *The Scaled Boundary Finite Element Method*. Chichester: John Wiley and Sons, 2003.

[4] J. Liu and G. Lin, "A scaled boundary finite element method applied to electrostatic problems," *Engineering Analysis with Boundary Elements*, vol. 36, pp.1721-1732, 2012.

[5] C. Li, H. Man, C. Song, and W. Gao, "Fracture analysis of piezoelectric materials using the scaled boundary finite element method," *Engineering Fracture Mechanics*, vol. 97, pp. 52-71, 2013.

[6] M. Li, H. Zhang, H. Guan, and G. Lin, "Three-dimensional investigation of wave–pile group interaction using the scaled boundary finite element method, Part I: Theoretical developments," *Ocean Engineering*, vol. 64, pp. 174-184, 2013.

[7] M. Li, H. Zhang, H. Guan, and G. Lin, "Three-dimensional investigation of wave–pile group interaction using the scaled boundary finite element method—Part II: Application results," *Ocean Engineering*, vol. 64, pp. 185-195, 2013.

[8] T. H. Vu and A. J. Deeks, "Using fundamental solutions in the scaled boundary finite element method to solve problems with concentrated loads," *Computational Mechanics*, vol. 53, pp. 641-657, 2014.

[9] E. T. Ooi, C. Song, F. Tin-Loi, and Z. J. Yang, "Automatic modelling of cohesive crack propagation in concrete using polygon scaled boundary finite elements," *Engineering Fracture Mechanics*, vol. 93, pp. 13-33, 2012.

[10] E. T. Ooi, C. Song, F. Tin-Loi, and Z. J. Yang, "Dynamic crack propagation simulation with scaled boundary polygon elements and automatic remeshing technique," *Engineering Fracture Mechanics*, vol. 106, pp. 1-21, 2013.

[11] C. Li, E. T. Ooi, C. Song, and S. Natarajan, "SBFEM for fracture analysis of piezoelectric composites under thermal load," *International Journal of Solids and Structures*, vol. 52, pp. 114-129, 2015.

[12] F. Li and P. Ren, "A novel solution for heat conduction problems by extending scaled boundary finite element method," *International Journal of Heat and Mass Transfer*, vol. 95, pp. 678-688, 2016.

[13] J. P. Wolf and C. Song, *Finite-Element Modelling of Unbounded Domain*. Chichester: Jonh Wiley and Sons, 1996.

[14] J. P. Wolf and C. Song, "Consistent infinitesimal finite-element cell method: in-plane motion," *Computer Methods in Applied Mechanics and Engineering*, vol. 123, pp. 355-370, 1995.

[15] J. P. Wolf and C. Song, "Unit-impulse response matrix of unbounded medium by infinitesimal finite-element cell method," *Computer Methods in Applied Mechanics and Engineering*, vol. 122, pp. 251-272, 1995.

[16] J. P Wolf and C. Song, "The scaled boundary finite-element method – A fundamental solution-less boundary-element method," *Computer Methods in Applied Mechanics and Engineering*, vol. 190, pp. 5551-5568, 2001.

[17] J. A. Deeks and P. J Wolf, "A virtual work derivation of the scaled boundary finite-element method for elastostatics," *Computational Mechanics*, vol. 28, pp. 489-504, 2002.

[18] A. J. Deeks, "Prescribed side-face displacements in the scaled boundary finite-element method," *Computers & Structures*, vol. 82, pp. 1153-1165, 2004.

[19] M. S. Chowdhury, C. Song, and W. Gao, "Probabilistic fracture mechanics with uncertainty in crack size and orientation using the scaled boundary finite element method," *Computers & Structures*, vol. 37, pp. 93-103, 2014.

[20] S. Dai, C. Augarde, C. Du, and D. Chen, "A fully automatic polygon scaled boundary finite element method for modelling crack propagation," *Engineering Fracture Mechanics*, vol. 133, pp. 163-178, 2015.

[21] S. Shrestha and M. Ohga, "Scaled boundary finite element method for various crack problems," *Steel Structures*, vol. 7, pp. 277-287, 2007.

[22] C. Song, F. Tin-Loi, and W. Gao, "Transient dynamic analysis of interface cracks in anisotropic bimaterials by the scaled boundary finite-element method," *International Journal of Solids and Structures*, vol. 47, pp. 978-989, 2010.

[23] J. P. Doherty and D. J Deeks, "Adaptive coupling of the finite-element and scaled boundary finite-element methods for non-linear analysis of unbounded media," *Computers and Geotechnics*, vol. 32, pp. 436-444, 2005.

[24] X. N. Meng and Z. J. Zou, "Radiation and diffraction of water waves by an infinite horizontal structure with a sidewall using SBFEM," *Ocean Engineering*, vol. 60, pp. 193-199, 2013.
[25] H. Gravenkamp, C. Birk, and C. Song, "The computation of dispersion relations for axisymmetric waveguides using the scaled boundary finite element method," *Ultrasonics*, vol. 54, pp. 1373-1385, 2014.
[26] M. Li, H. Zhang, and H. Guan, "Study of offshore monopole behavior due to ocean waves," *Ocean Engineering*, vol. 38, pp. 1946-1956, 2011.
[27] A. J. Deeks and J. P. Wolf, "An h-hierarchical adaptive procedure for the scaled boundary finite-element method," *International Journal for Numerical Methods in Engineering*, vol. 54, pp. 585-605, 2002.
[28] T. H. Vu, and A. J. Deeks, "Use of higher-order shape functions in the scaled boundary finite element method," *International Journal for Numerical Methods in Engineering*, vol. 65, pp. 1714-1733, 2006.
[29] A. J. Deeks and C. E. Augarde, "A meshless local Petrov-Galerkin scaled boundary method," *Computer Mechanics*, vol. 36, pp. 159-170, 2005.
[30] T. H. Vu and A. J. Deeks, "A p-adaptive scaled boundary finite element method based on maximization of the error decrease rate," *Computational Mechanics*, vol. 41, pp. 441-455, 2008.
[31] Y. He, H. Yang and A. J. Deeks, "An Element-free Galerkin (EFG) scaled boundary method," *Finite Elements in Analysis and Design*, vol. 62, pp. 28-36, 2012.
[32] Y. He, H. Yang, and A. J. Deeks, "Use of Fourier shape functions in the scaled boundary method," *Engineering Analysis with Boundary Elements*, vol. 41, pp. 152-159, 2014.
[33] R. Dieringer and W. Becker, "A new scaled boundary finite element formulation for the computation of singularity orders at cracks and notches in arbitrarily laminated composites," *Composite Structures*, vol. 123, pp. 263-270, 2015.
[34] C. Li, C. Song, H. Man, E. T. Ooi, and W. Gao, "2D dynamic analysis of cracks and interface cracks in piezoelectric composites using the SBFEM," *International Journal of Solids and Structures*, vol. 51, pp. 2096-2108, 2014.
[35] Y. He, H. Yang, M. Xu and A. J. Deeks, "A scaled boundary finite element method for cyclically symmetric two-dimensional elastic analysis," *Computers & Structures*, vol. 120, pp. 1-8, 2013.
[36] M. H. Sadd, *Elasticity: Theory, Applications, and Numerics*. Academic Press, 2014, pp. 181-182.